



**HAL**  
open science

# Angular momentum and chemical transport by azimuthal magnetorotational instability in radiative stellar interiors

Domenico G. Meduri, Laurène Jouve, François Lignières

► **To cite this version:**

Domenico G. Meduri, Laurène Jouve, François Lignières. Angular momentum and chemical transport by azimuthal magnetorotational instability in radiative stellar interiors. *Astronomy and Astrophysics* - A&A, 2024, 683, pp.A12. 10.1051/0004-6361/202347672 . hal-04484757

**HAL Id: hal-04484757**

**<https://hal.science/hal-04484757>**

Submitted on 29 Feb 2024

**HAL** is a multi-disciplinary open access archive for the deposit and dissemination of scientific research documents, whether they are published or not. The documents may come from teaching and research institutions in France or abroad, or from public or private research centers.

L'archive ouverte pluridisciplinaire **HAL**, est destinée au dépôt et à la diffusion de documents scientifiques de niveau recherche, publiés ou non, émanant des établissements d'enseignement et de recherche français ou étrangers, des laboratoires publics ou privés.

# Angular momentum and chemical transport by azimuthal magnetorotational instability in radiative stellar interiors

Domenico G. Meduri<sup>1,2</sup> , Laurène Jouve<sup>1,2</sup> , and François Lignières<sup>1</sup> 

<sup>1</sup> IRAP, Université de Toulouse, CNRS, CNES, UPS, 14 avenue Edouard Belin, 31400 Toulouse, France  
e-mail: [domenico.meduri@irap.omp.eu](mailto:domenico.meduri@irap.omp.eu)

<sup>2</sup> Leibniz-Institut für Astrophysik Potsdam (AIP), An der Sternwarte 16, 14482 Potsdam, Germany

Received 7 August 2023 / Accepted 26 November 2023

## ABSTRACT

**Context.** The transport of angular momentum and chemical elements within evolving stars remains poorly understood. Asteroseismic and spectroscopic observations of low-mass main sequence stars and red giants reveal that their radiative cores rotate orders of magnitude slower than classical predictions from stellar evolution models and that the abundances of their surface light elements are too small. Magnetohydrodynamic (MHD) turbulence is considered a primary mechanism to enhance the transport in radiative stellar interiors but its efficiency is still largely uncertain.

**Aims.** We explore the transport of angular momentum and chemical elements due to azimuthal magnetorotational instability, one of the dominant instabilities expected in differentially rotating radiative stellar interiors.

**Methods.** We employed 3D MHD direct numerical simulations in a spherical shell of unstratified and stably stratified flows under the Boussinesq approximation. The background differential rotation was maintained by a volumetric body force. We examined the transport of chemical elements using a passive scalar.

**Results.** We provide evidence of magnetorotational instability for purely azimuthal magnetic fields in the parameter regime expected from local and global linear stability analyses. Without stratification and when the Reynolds number  $Re$  and the background azimuthal field strength are large enough, we observed dynamo action driven by the instability at values of the magnetic Prandtl number  $Pm$  in the range 0.6–1, which is the smallest ever reported in a global setup. When considering stable stratification at  $Pm = 1$ , the turbulence is transitional and becomes less homogeneous and isotropic upon increasing buoyancy effects. The transport of angular momentum occurs radially outward and is dominated by the Maxwell stresses when stratification is large enough. We find that the turbulent viscosity decreases when buoyancy effects strengthen and scales with the square root of the ratio of the reference rotation rate  $\Omega_a$  to the Brunt–Väisälä frequency  $N$ . The chemical turbulent diffusion coefficient scales with stratification similarly to the turbulent viscosity, but is lower in amplitude so that the transport of chemicals is slower than the one of angular momentum, in agreement with recent stellar evolution models of low-mass stars.

**Conclusions.** We show that the transport induced by azimuthal magnetorotational instability scales somewhat slowly with stratification and may enforce rigid rotations of red giant cores on a timescale of a few thousand years. In agreement with recent stellar evolution models of low-mass stars, the instability transports chemical elements less efficiently than angular momentum.

**Key words.** instabilities – magnetohydrodynamics (MHD) – turbulence – methods: numerical – stars: interiors – stars: rotation

## 1. Introduction

A consistent description of the transport of angular momentum (AM) and chemical elements within evolving stars is still lacking and remains a major problem for stellar physics. Recent asteroseismic observations based on space photometry have transformed our knowledge of the dynamics of stellar interiors, offering the opportunity for unprecedented advances in this field. By uncovering the internal rotations of low-mass stars at various stages of evolution, from main sequence (MS) stars to white dwarf remnants, these observations unambiguously showed that the cores of these stars rotate orders of magnitude slower than classical predictions from stellar evolution models and that AM is efficiently extracted from stellar cores as they evolve (for a recent review, see [Aerts et al. 2019](#)). For instance, the radiative cores of low-mass subgiants rotate slowly and do not spin up while evolving on the red giant branch ([Beck et al. 2011](#); [Deheuvels et al. 2014](#); [Gehan et al. 2018](#)). The cores of these stars are in gravitational contraction and, if AM was conserved, they would rotate almost 3 orders of magnitude faster and spin up while evolving (e.g., [Cantiello et al. 2014](#)). The convective envelopes, on the other hand, expand and should spin down lead-

ing to a strong rotation contrast with the core. The measured envelope rotation rates of subgiants are instead only less than 10 times slower than those of the cores at most ([Deheuvels et al. 2014](#)). Red giants are also the sole class of stellar objects for which, since as of recently, we have direct seismic measurements of their internal magnetic fields ([Li et al. 2022, 2023](#); [Deheuvels et al. 2023](#)). The seismic detection probes a narrow region of the core around to the hydrogen burning shell where strong radial field strengths ranging from 30 to 600 kG have been reported.

In order to explain all of these observations, various mechanisms to enhance the transport of AM in radiative stellar interiors have been proposed. The transport by atomic diffusion and standard hydrodynamical processes, such as meridional circulation and shear instabilities, falls short of predicting the almost rigid rotation of the Sun's core, as well as the slow internal rotations of red giants and white dwarfs (e.g., [Eggenberger et al. 2012](#); [Marques et al. 2013](#); [Dumont et al. 2021](#)). Internal gravity waves, which are excited by convective motions in the overlying envelope, can contribute to transport AM in the cores of solar-type stars and subgiants, but the process is likely negligible on the red giant branch ([Fuller et al. 2014](#); [Pinçon et al. 2017](#)).

The transport by instabilities due to magnetic fields is expected to be higher than any of the hydrodynamical processes above and is considered the primary mechanism to explain the slow internal rotations observed (Spruit 2002; Cantiello et al. 2014; Spada et al. 2016; Fuller et al. 2019). In differentially rotating radiative stellar interiors, magnetorotational instability and Tayler instability are expected to be the two dominant magnetohydrodynamic (MHD) instabilities (Spruit 1999).

Magnetorotational instability (MRI) is an instability of hydrodynamically stable shear flows in which the magnetic field allows the free energy of the shear to be released. For axisymmetric magnetic fields that are either purely azimuthal or with both toroidal and poloidal components, linearly unstable MRI modes are nonaxisymmetric (e.g., Balbus & Hawley 1992; Ogilvie & Pringle 1996; Rüdiger et al. 2007; Hollerbach et al. 2010). Dominant toroidal fields are expected in differentially rotating radiative stellar interiors, provided that the poloidal field is weak enough (Spruit 1999). Azimuthal MRI (AMRI) generally refers to the instability of hydrodynamically stable Taylor–Couette flow, the flow of a viscous incompressible fluid confined between two coaxial and rigidly rotating cylinders, with imposed current-free azimuthal fields (Rüdiger et al. 2007; Kirillov et al. 2012). In this work, however, we refer to this version of the instability for generic, purely or dominantly azimuthal field configurations with a nonzero Lorentz force that are free to evolve over time, as expected in astrophysical situations. Due to its non-axisymmetric nature, AMRI can self-sustain a magnetic field (e.g., Guseva et al. 2017a). Dynamo action driven by MRI is a highly nonlinear phenomenon in which the turbulence due to the instability generates large-scale magnetic fields that continuously destabilize the flow to self-sustain the turbulence (Rincon 2019).

Taylor instability (TI) is instead a kink-type instability of purely axisymmetric azimuthal fields driven by magnetic pressure gradients (Tayler 1973). This instability is expected to dominate in radiative stellar interiors since, relying on almost horizontal motions, is less sensitive than MRI to stable stratification (Spruit 1999; Bonanno & Urpin 2012). However, numerical simulations show that the presence of a latitudinal shear may favor AMRI over TI, even when stable stratification is relatively high (Jouve et al. 2020). While there has been no asteroseismic evidence of latitudinal differential rotation in the interior of evolved stars so far, theoretical studies suggest that this can be produced by gravitational contraction when buoyancy effects are not too high, as for example in the outer radiative regions of red giants (Gouhier et al. 2021, 2022). Numerical simulations in a spherical shell have also demonstrated that MRI can occur for dominantly azimuthal fields generated by shearing an initial weak poloidal field through differential rotation, a process known as the  $\Omega$ -effect and that is thought to take place in stellar interiors (Jouve et al. 2015; Meduri et al. 2019).

In spite of its importance, the efficiency of the AM transport due to AMRI in radiative stellar interiors remains highly uncertain. AMRI-induced transport is mostly investigated using shearing box simulations, which are local numerical models of accretion disks hardly relevant to stellar interiors (e.g., Lesur & Longaretti 2007). Global numerical studies generally model liquid metal laboratory experiments, hence consider unstratified Taylor–Couette flow with imposed magnetic fields (e.g., Rüdiger et al. 2013; Guseva et al. 2017b). Numerical simulations of stratified AMRI turbulence in a spherical geometry can certainly provide more robust constraints on the transport in stellar interiors. However, there are only a few of these studies, which either explore a very limited range of

parameters (Arlt et al. 2003), often relevant to neutron stars (Reboul-Salze et al. 2022), or focus only on the role played by differential rotation (Jouve et al. 2020).

Stellar evolution models can provide indication of the efficiency of the missing transport processes. However, in the AM evolution equation of these models, the turbulence is often parameterized with a diffusion coefficient, which is used as a free parameter to fit the observations. This procedure ignores the physical origin of the transport and how this scales with the fundamental fluid properties, such as stratification or the molecular diffusivities, which strongly vary in the interior of stars and during their evolution. For example, a turbulent diffusion coefficient depending on the ratio of the core to surface rotation rates, attributed by analogy to the expected scaling of AMRI turbulence with the shear, and that increases monotonically from about  $10^2 \text{ cm}^2 \text{ s}^{-1}$  to almost  $10^6 \text{ cm}^2 \text{ s}^{-1}$  has been shown to reproduce the rotational evolution of subgiants and red giants (Spada et al. 2016; Moyano et al. 2022, 2023). As for TI turbulence, theoretical scaling laws for the enhanced turbulent viscosity have instead been employed in stellar evolution models (Fuller et al. 2019) but they fail at capturing the rotational evolution of subgiants and red giants simultaneously (Eggenberger et al. 2019).

Advancing our understanding of the AM transport in stellar interiors is also key to comprehend the mixing of chemical elements. The transport of light elements such as lithium, beryllium and boron, which are destroyed at temperatures as low as a few million K, contributes to determine the chemical composition and, consequently, the stellar evolution (Deliyannis et al. 2000). State-of-the-art stellar evolution models including atomic diffusion and hydrodynamical transport processes such as those mentioned above predict surface abundances of  ${}^7\text{Li}$  (Li hereafter) orders of magnitude higher than those observed for the Sun and solar-type stars (Lodders et al. 2009; Dumont et al. 2021), and also for red giants (see Charbonnel et al. 2020 and references therein). Recent progresses on understanding the combined rotational and chemical evolution of stars again come from considering the transport due to MHD turbulence. For example, stellar evolution models suggest that TI-induced transport may reconcile the almost rigid rotation of the Sun’s core and its photospheric Li abundance (Eggenberger et al. 2022) and that MRI turbulence strongly influences the chemical evolution of massive stars (Wheeler et al. 2015; Griffiths et al. 2022). These studies, however, employ uncertain theoretical prescriptions of TI-driven dynamo action or somewhat approximate estimates of MRI-induced transport derived from accretion disk simulations. MHD numerical simulations appropriate to model stellar interiors and that explicitly explore the transport of chemicals could provide better constraints but such studies are lacking so far.

In this work we investigate the transport of AM and chemical elements due to AMRI turbulence using 3D direct numerical simulations in a spherical shell. We consider unstratified and stably stratified flows under the Boussinesq approximation where the background differential rotation is forced. We perform a comprehensive parametric study varying the rotation rate, the molecular diffusivities and stratification. The molecular diffusivity ratios are among the lowest ones ever explored in a global geometry for MRI turbulence and are relevant to the electron-degenerate cores of red giants. A passive scalar allows us to examine the transport of chemical elements.

The remainder of this work is organized as follows. In Sect. 2 we describe the governing equations and the numerical model. The unstratified axisymmetric solutions, obtained from the evolution of an initial purely azimuthal field, are discussed

in Sect. 3. Section 4 investigates their stability to weak nonaxisymmetric perturbations. In Sect. 5 we describe the nonlinear evolution of the unstable solutions where AMRI is identified and discuss the effect of stable stratification. Section 6 explores and quantifies the transport of AM and Sect. 7 the one of a passive scalar. Section 8 closes the paper with a discussion of the numerical results and their application to stellar interiors.

## 2. Governing equations

We consider a stably stratified MHD flow under the Boussinesq approximation. The fluid is confined to a spherical shell of thickness  $d = r_o - r_i$ , where  $r_i$  and  $r_o$  are the inner and outer boundary radii respectively, and has uniform kinematic viscosity  $\nu$ , magnetic diffusivity  $\eta$ , and thermal diffusivity  $\kappa$ . The thermal expansion coefficient is  $\alpha$ . The density of the fluid  $\rho$  is uniform, hence gravity varies linearly with radius,  $\mathbf{g} = -g_o r/r_o \hat{\mathbf{e}}_r$ , where  $g_o$  is the gravitational acceleration at the outer boundary. If not explicitly stated otherwise,  $(r, \theta, \phi)$  denote dimensionless spherical coordinates hereafter and the respective unit vectors are  $\hat{\mathbf{e}}_r$ ,  $\hat{\mathbf{e}}_\theta$ , and  $\hat{\mathbf{e}}_\phi$ .

The governing equations are non-dimensionalized using the shell gap  $d$  as length scale and  $\tau_\Omega = 1/\Omega_a$  as timescale, where  $\Omega_a$  is the angular velocity at the cylindrical radius  $s = r \sin \theta = 0$ . The scale for temperature is  $\Delta T = T_o - T_i > 0$ , the imposed positive temperature contrast between the isothermal outer and inner boundaries that establishes stable stratification. The non-hydrostatic pressure  $\Pi$  is scaled by  $\rho d \Omega_a^2$  and the magnetic field  $\mathbf{B}^*$  by  $(\mu_0 \rho)^{1/2} d \Omega_a$ , where  $\mu_0$  is the magnetic permeability of vacuum. This choice makes the dimensionless magnetic field strength  $B$  equal to the Lenhart number

$$\text{Le} = \frac{B^*}{(\mu_0 \rho)^{1/2} d \Omega_a}, \quad (1)$$

which can be interpreted as the ratio of the rotation timescale  $\tau_\Omega$  to the Alfvén travel time  $d/u_A$ , where  $u_A = B^*/(\mu_0 \rho)^{1/2}$  is the Alfvén velocity. In the following we use  $B$  and  $\text{Le}$  interchangeably. For example, the dimensionless azimuthal field will be indicated with  $B_\phi$  or  $\text{Le}_\phi$ .

In this scaling scheme, the equations governing the evolution of the fluid velocity  $\mathbf{u}$ , the magnetic field  $\mathbf{B}$ , and the temperature perturbations  $T'$  (around the background adiabatic state) are: the momentum equation

$$\frac{\partial \mathbf{u}}{\partial t} + (\mathbf{u} \cdot \nabla) \mathbf{u} = -\nabla \Pi - \frac{N^2}{\Omega_a^2} T' \frac{r}{r_o} \hat{\mathbf{e}}_r + (\nabla \times \mathbf{B}) \times \mathbf{B} + \frac{1}{\text{Re}} \nabla^2 \mathbf{u} + \mathbf{f}, \quad (2)$$

the induction equation

$$\frac{\partial \mathbf{B}}{\partial t} = \nabla \times (\mathbf{u} \times \mathbf{B}) + \frac{1}{\text{Re Pm}} \nabla^2 \mathbf{B}, \quad (3)$$

and the evolution equation for the temperature perturbations

$$\frac{\partial T'}{\partial t} + (\mathbf{u} \cdot \nabla) T' = \frac{1}{\text{Re Pr}} \nabla^2 T'. \quad (4)$$

The flow and the magnetic field obey to the continuity conditions

$$\nabla \cdot \mathbf{u} = 0 \quad \text{and} \quad \nabla \cdot \mathbf{B} = 0. \quad (5)$$

The four dimensionless control parameters of the problem are: the Reynolds number

$$\text{Re} = \frac{\Omega_a d^2}{\nu}, \quad (6)$$

the ratio of the reference Brunt–Väisälä frequency  $N$  to the reference rotation rate  $\Omega_a$ ,

$$\mathcal{N} = \frac{N}{\Omega_a} = \left( \frac{\alpha \Delta T g_o}{d} \right)^{1/2} \frac{1}{\Omega_a}, \quad (7)$$

the Prandtl number

$$\text{Pr} = \frac{\nu}{\kappa}, \quad (8)$$

and the magnetic Prandtl number

$$\text{Pm} = \frac{\nu}{\eta}. \quad (9)$$

In this work we fix the aspect ratio of the spherical shell  $\chi = r_i/r_o$  to 0.3. We employ stress-free boundary conditions for the flow. Electrically insulating boundary conditions are assumed for the magnetic field, which are appropriate to match a potential field outside the fluid volume.

The azimuthal body force

$$\mathbf{f} = \frac{u_f - \bar{u}_\phi}{\tau} \hat{\mathbf{e}}_\phi \quad (10)$$

in Eq. (2) imposes the background axisymmetric differential rotation. Here  $\bar{u}_\phi$  is the axisymmetric azimuthal velocity and  $u_f = s \Omega_f$  is the forced contribution, which is axisymmetric ( $\partial u_f / \partial \phi = 0$ ). The timescale  $\tau$  in Eq. (10) provides the time on which  $\bar{u}_\phi$  relaxes to  $u_f$  and is fixed to  $5 \times 10^{-3}$ . This is the shortest timescale in the system and practically sets the numerical integration time step in our simulations.

The forced angular velocity  $\Omega_f$  is vertically invariant and is defined by

$$\Omega_f = 2\mu - 1 + \frac{2(1-\mu)}{1 + (1-\chi)^b s^b}, \quad (11)$$

where  $\mu = \Omega_e/\Omega_a < 1$ . Here  $\Omega_e$  is the angular velocity at the equator on the outer boundary. The real constant  $b > 0$  defines the steepness of the decay of  $\Omega_f$  with the cylindrical radius  $s$ . In this work we consider  $\mu = 0.45$  and  $b = 2.9$ . The black line in Fig. 1a shows  $\Omega_f$  as a function of the cylindrical radius  $s$  for this parameter combination. Figure 1b presents a snapshot of the axisymmetric angular velocity  $\bar{\Omega}$  in one of our numerical simulations and demonstrates that this closely follows the forced angular velocity  $\Omega_f$ .

The forced angular velocity that we choose here simultaneously maximizes the mean and the maximum of the shear parameter  $q = |d \ln \Omega_f / d \ln s|$  in the fluid domain while still maintaining the flow stable according to the Rayleigh criterion for inviscid flows, which prescribes  $\partial L^2 / \partial s > 0$ , where  $L = s \bar{u}_\phi$  is the specific AM. In the unstratified case, that is when  $\mathcal{N} = 0$  and there is no temperature equation to solve, we verified numerically that this flow is indeed hydrodynamically stable to weak nonaxisymmetric perturbations by performing nonmagnetic runs at the typical Reynolds numbers  $\text{Re}$  explored here. The shear parameter  $q$  increases monotonically with  $s$  and attains its maximum value on the outer boundary at the equator where  $q \approx 1.77$  (Fig. 1a, red line). The mean value of  $q$  in the domain is 0.57. It is useful to define a characteristic timescale and length scale of the shear. The shear timescale is  $\tau_{\Delta\Omega} = \Delta\Omega^{-1}$ , where  $\Delta\Omega = \Omega_a - \Omega_e = (1-\mu)\Omega_a \approx \Omega_a/2$  is the difference between the axial and the equatorial rotation rates. The shear length scale is  $l_{\Delta\Omega} = (\Omega_f^{-1} d\Omega_f/ds)^{-1}$ , which can be estimated as  $l_{\Delta\Omega} \sim (\Omega_e^{-1} \Delta\Omega/r_o)^{-1} = r_o/(\mu^{-1} - 1) \approx r_o$ .

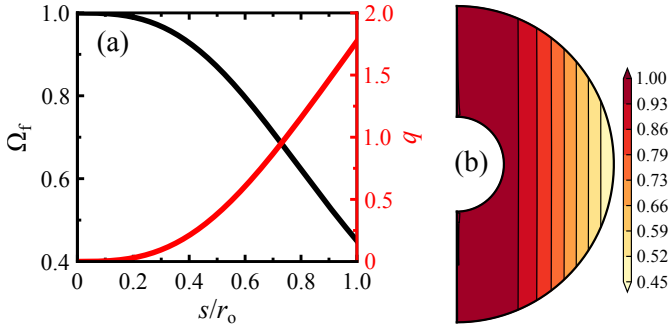


**Fig. 1.** Forced angular velocity employed in the simulations. (a) Forced angular velocity  $\Omega_f$  (Eq. (11) with  $\mu = 0.45$  and  $b = 2.9$ ) and shear parameter  $q$  as a function of the cylindrical radius  $s/r_0$ . (b) Snapshot of the axisymmetric angular velocity  $\bar{\Omega}$  in the axisymmetric simulation run at  $\mathcal{N} = 0$ ,  $\text{Re} = 5 \times 10^4$ ,  $\text{Pm} = 1$ , and  $\text{Le}_0 = 0.1$ .

The problem above is solved numerically using the open-source pseudospectral MHD code MagIC<sup>1</sup> (Wicht 2002; Schaeffer 2013), which we modified to include the volumetric body force  $\mathbf{f}$  in the momentum equation. The numerical technique is described in detail in Christensen & Wicht (2007) and we therefore mention only the essentials here. MagIC uses a poloidal-toroidal decomposition for the vector fields  $\mathbf{u}$  and  $\mathbf{B}$  and for the scalar temperature field. Spherical harmonics are employed in the latitudinal and azimuthal directions and Chebyshev polynomials in radius. An implicit-explicit time stepping scheme, where the nonlinear terms and the volumetric body force are treated explicitly, is employed. The nonaxisymmetric simulations performed here typically use a spatial resolution of 257 radial grid points and a maximum spherical harmonic (SH) degree  $\ell_{\text{max}} = 341$ . Depending on the characteristic scales of the turbulence to resolve, the spatial grid is sometimes coarser. The spherical harmonic kinetic and magnetic energy spectra of the solutions span at least three orders of magnitude in amplitude, which ensures numerical convergence of the results as we generally verified.

Throughout this work, we use the following notation for azimuthal, horizontal (over a spherical surface), and temporal averages of an arbitrary function  $f = f(r, \theta, \phi, t)$ ,

$$\bar{f} = \frac{1}{2\pi} \int_0^{2\pi} f \, d\phi,$$

$$\langle f \rangle = \frac{1}{4\pi r^2} \int_0^\pi \int_0^{2\pi} f r^2 \sin \theta \, d\phi \, d\theta,$$

and

$$\hat{f} = \frac{1}{\Delta t} \int_{t_1}^{t_1 + \Delta t} f \, dt$$

respectively. Here  $\Delta t$  is the time averaging period. In the following, only when explicitly specified, the angular brackets  $\langle \cdot \rangle$  denote spatial averages different from the one above. The nonaxisymmetric flow velocity and magnetic field are denoted by the superscript  $'$ , for example  $\mathbf{B}' = \mathbf{B} - \bar{\mathbf{B}}$ .

### 3. Unstratified axisymmetric solutions

We first describe the axisymmetric solutions obtained for an unstratified flow, that is when  $\mathcal{N} = 0$  and there is no temperature equation to solve.

<sup>1</sup> <https://magic-sph.github.io>

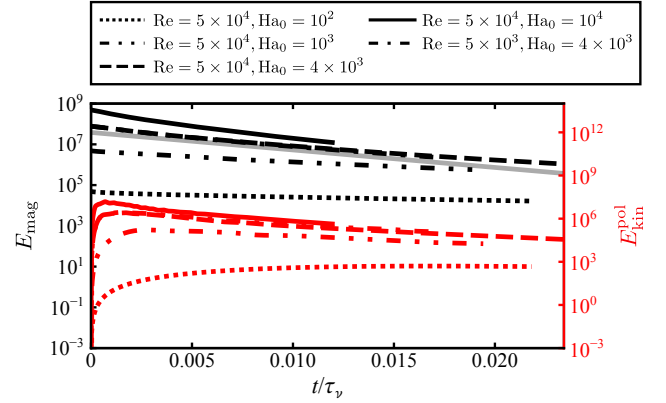


**Fig. 2.** Temporal evolution of the magnetic energy  $E_{\text{mag}}$  (black lines) and of the poloidal kinetic energy  $E_{\text{kin}}^{\text{pol}}$  (red lines) in five unstratified axisymmetric runs at different  $\text{Re}$  and  $\text{Ha}_0$  (see the legend at the top). The magnetic Prandtl number  $\text{Pm}$  is 1. Time is scaled with the viscous diffusion time  $\tau_v$ , here. Note that the left and right vertical axes span different ranges. The gray line displays the exponential Ohmic decay rate based on  $\eta/L_B^2$  for the run at  $\text{Re} = 5 \times 10^4$  and  $\text{Ha}_0 = 4 \times 10^3$  (see the main text for details).

#### 3.1. Initial magnetic field condition and dimensionless parameters

As initial condition for the magnetic field, we consider a purely azimuthal field linearly increasing with the cylindrical radius  $s$ ,

$$\mathbf{B}(t = 0) = B_0 s \hat{e}_\phi, \quad (12)$$

where  $B_0 = \text{Le}_0 = B_0^*/(\mu_0 \rho)^{1/2} d \Omega_a$  is the field strength at  $s = 1$ . In differentially rotating radiative stellar interiors where a weak axisymmetric poloidal field  $\bar{\mathbf{B}}_p$  is present, we expect dominantly azimuthal field configurations to be generated by the  $\Omega$ -effect, that is by shearing the poloidal field through the differential rotation via the term  $s(\bar{\mathbf{B}}_p \cdot \nabla)\Omega$  in the azimuthal component of the axisymmetric induction equation (e.g., Spruit 1999). The azimuthal field would be stronger where the differential rotation is higher and, given our background angular velocity profile  $\Omega_f$ , this motivates the choice of the initial condition above.

To discuss the axisymmetric solutions, it is useful to rescale the magnetic field independently of the rotation rate by introducing the Hartmann number

$$\text{Ha} = \frac{B^* d}{(\mu_0 \rho \nu \eta)^{1/2}}. \quad (13)$$

The Hartmann number is related to the dimensionless parameters introduced in the previous section by  $\text{Ha} = \text{Le} \text{Re} \text{Pm}^{1/2}$  and can be interpreted as the ratio of the geometric mean of the viscous and magnetic diffusion times,  $\tau_v = d^2/\nu$  and  $\tau_\eta = d^2/\eta$  respectively, to the Alfvén travel time  $d/u_A$ . In the following  $\text{Ha}_0$  and  $\text{Ha}_\phi$  denote the Hartmann number based on the initial reference field strength  $B_0^*$  and on the azimuthal field  $B_\phi^*$  respectively.

In Sect. 3.2 we discuss the flow and magnetic field solutions obtained when varying  $\text{Ha}_0$  and the Reynolds number  $\text{Re}$  at a fixed magnetic Prandtl number  $\text{Pm}$  of 1. For consistency with the new dimensionless magnetic field  $\bar{\mathbf{B}} = \text{Ha}$ , the flow velocity is scaled with  $d/(\nu \eta)^{1/2}$  and indicated with  $\bar{u}$  in this section.

#### 3.2. Temporal evolution

The black lines in Fig. 2 illustrate the temporal evolution of the volume integrated magnetic energy  $E_{\text{mag}} = \frac{1}{2} \int \bar{\mathbf{B}}^2 dV$  in four

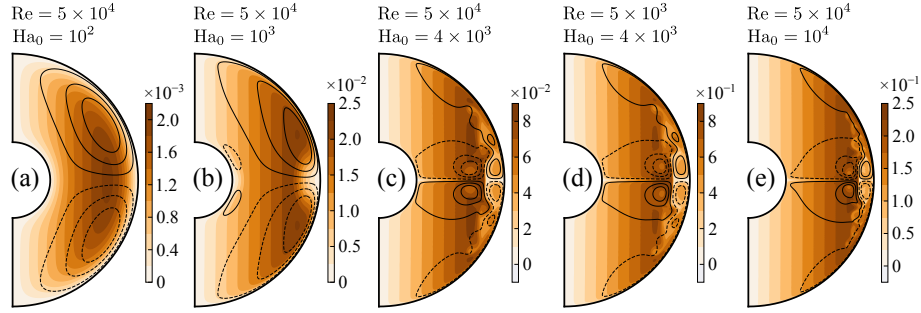


**Fig. 3.** Unstratified axisymmetric solutions of the runs in Fig. 2 at the times when the poloidal kinetic energy  $E_{\text{kin}}^{\text{pol}}$  reaches its maximum. The Reynolds number  $\text{Re}$  and the Hartmann number  $\text{Ha}_0$  are shown at the top of each panel. The magnetic Prandtl number  $\text{Pm}$  is 1. The colour contours show the azimuthal magnetic field  $Le_\phi$  and the black isocontour lines the meridional circulation (solid and dashed for clockwise and counterclockwise, respectively).

runs at  $\text{Re} = 5 \times 10^4$  with  $\text{Ha}_0$  in the range  $10^2$ – $10^4$  and in one run at the lower  $\text{Re}$  of  $5 \times 10^3$ . Since no poloidal field is initialized, the solution remains purely toroidal. Axisymmetric magnetic fields cannot be maintained by dynamo action (Cowling’s antidymano theorem) and the toroidal field decays exponentially due to Ohmic diffusion. The magnetic energy evolution is compatible with a field decay rate of  $\eta/l_B^2$ , where  $l_B$  is the characteristic azimuthal field length scale, which we calculated as a meridional average of  $|\tilde{B}_\phi|/|\nabla\tilde{B}_\phi|$  at the last numerical integration time step of these runs (the gray line in Fig. 2 shows the exponential Ohmic decay rate of the run at  $\text{Re} = 5 \times 10^4$  and  $\text{Ha}_0 = 4 \times 10^3$  as an example).

Due to the azimuthal flow forcing, the toroidal kinetic energy  $E_{\text{kin}}^{\text{tor}} = \frac{1}{2} \int \tilde{u}_\phi^2 dV \approx \frac{1}{2} \int \tilde{u}_r^2 dV$ , which is approximately  $5.75 \times 10^9$  and  $5.75 \times 10^7$  in the runs at  $\text{Re} = 5 \times 10^4$  and  $5 \times 10^3$  respectively, is the dominant energy contribution and remains constant over time (not shown). Boundary driven flows produced by the Lorentz force induce a global meridional circulation in the first few rotation times  $\tau_\Omega$ , as evidenced by the initial rapid growth of the poloidal kinetic energy  $E_{\text{kin}}^{\text{pol}}$  (red lines in Fig. 2). The peak amplitude of  $E_{\text{kin}}^{\text{pol}}$  scales with  $\text{Ha}_0^2$  and, on longer times,  $E_{\text{kin}}^{\text{pol}}$  decays at a rate comparable to the one of the field, confirming the magnetic origin of the meridional flow. We now describe qualitatively how this global circulation is generated and how its morphology changes when varying  $\text{Ha}_0$ .

The jump between the interior azimuthal field solution  $\tilde{B}_\phi \propto s$  and the electrically insulating boundary conditions, which impose  $\tilde{B}_\phi = 0$  at  $r = r_i/d$  and  $r_o/d$ , is accommodated in thin layers close to the boundaries, where the radial Lorentz force is strong due to the high radial gradients of the field. Due to the form of the interior field solution, the radial Lorentz force is stronger in the outer boundary layer than in the inner one. The Lorentz force in these boundary layers induces radial flows which, by mass conservation, generate return flows in the latitudinal direction. These return flows remain high in amplitude due to the stress-free boundary conditions and induce the large scale circulation observed. We note that the Lorentz force plays a similar dynamical role in modifying viscous boundary layers when a transverse magnetic field is applied (Hartmann boundary layers; see, e.g., Dormy & Soward 2007).

The boundary driven circulation is equatorially antisymmetric and, at the time when the poloidal kinetic energy peaks, is characterized by one cell in each hemisphere for the run at the lowest  $\text{Ha}_0$  of  $10^2$  (black isocontours in Fig. 3a). Increasing  $\text{Ha}_0$  to  $10^3$ , the outer boundary layer thickness decreases as expected (black isocontours in Fig. 3b) and the meridional circulation amplitude strengthen (Fig. 2, dash double-dot red line). The radial Lorentz force is now important in the inner boundary layer

as well, producing secondary circulation cells in the inner fluid regions (Fig. 3b). These secondary circulation cells are characterized by flows in the opposite direction to those of the primary ones, due to the opposite sign of the driving radial Lorentz force in the inner and outer boundary layers.

At  $\text{Ha}_0 \gtrsim 4 \times 10^3$ , the circulation driven by the inner boundary layer extends toward the outer fluid regions and becomes comparable in amplitude to the outer one (black isocontours in Figs. 3c,e). The azimuthal field is efficiently advected by such strong flows and complex configurations with locally strong field gradients are produced (Figs. 3c,e).

Further evidence that the meridional flow in our simulations is of magnetic origin is given by the fact that the solution does not depend on  $\text{Re}$ . The evolution of the magnetic and kinetic energies of the two runs at  $\text{Ha}_0 = 4 \times 10^3$  in Fig. 2 with  $\text{Re} = 5 \times 10^3$  (dotted-dashed line) and  $5 \times 10^4$  (dashed line) are indeed almost identical and snapshots of the two solutions are nearly indistinguishable (Figs. 3c,d). While the axisymmetric solutions above may be regarded as peculiar, they have to be considered only as initial states prone to AMRI. These solutions support turbulence for a period long enough to study the transport of AM and chemical elements, as we shall see in the following.

## 4. Linear stability

We now investigate the stability of the unstratified axisymmetric solutions discussed in the previous section. We introduce non-axisymmetric perturbations after the magnetically driven meridional flows develop and the azimuthal field slowly decays due to Ohmic diffusion. The perturbations consist of a spatially uncorrelated random nonaxisymmetric toroidal field of weak amplitude. This is obtained by adding to the spherical harmonic decomposition of the toroidal field and for each radii small amplitude coefficients  $\delta h_{\ell,m}(r)$  drawn from a uniform distribution for all degrees  $\ell$  and orders  $m > 0$ . As in the previous section, the magnetic Prandtl number  $\text{Pm}$  is fixed to 1 here. The Reynolds number  $\text{Re}$  is varied in the range  $10^3$ – $10^5$ . At a fixed  $\text{Re}$ , to explore the effect of the background azimuthal field strength on the stability, we either perform runs with different  $\text{Ha}_0$  or we introduce the perturbations at successive times in a single run. The azimuthal field strength of the perturbed axisymmetric solution is characterized by the maximum value of  $\text{Ha}_\phi$  in the fluid domain at the perturbation time  $t = t_{\text{pert}}$ . This is indicated as  $\text{Ha}_\phi^{\text{max}}$  hereafter and ranges from 60 to about  $10^4$ .

### 4.1. Parameter space for stable and unstable regimes

Hydrodynamically stable shear flows with purely axisymmetric azimuthal fields as those considered here are stable to

axisymmetric perturbations (Velikhov 1959), but they can be unstable to AMRI and to TI. At fixed  $Re$ , AMRI can develop only if the azimuthal field is not too weak nor too strong, otherwise AMRI modes are stabilized by diffusive effects or by magnetic tension respectively. We provide order of magnitude estimates of these stability limits using results from the local linear stability analysis of Masada et al. (2006). The authors employ cylindrical coordinates and consider classical local harmonic perturbations with an azimuthal wavelength much larger than the meridional ones. The azimuthal velocity  $u_\phi = s\Omega$  and the toroidal field  $B_\phi$  of the basic, purely toroidal axisymmetric state are assumed to depend only on the cylindrical radius  $s$ . For an unstratified flow with strong differential rotation, as in most of our numerical simulations where  $q \gg Le_\phi^2$ , the most unstable azimuthal mode predicted by the local linear analysis is

$$m_{\max}^{\text{AMRI}} = \frac{(4q - q^2)^{1/2} \Omega}{2 \omega_A} \quad (14)$$

in the absence of diffusive effects. Here  $\omega_A = B_\phi / (\mu_0 \rho)^{1/2} s$  is the local azimuthal Alfvén frequency. The adiabatic growth rate of the most unstable mode is

$$\gamma_{\max}^{\text{AMRI}} = \frac{q \Omega}{2}. \quad (15)$$

AMRI can develop only when its most unstable mode grows faster than it decays by resistive effects (or equivalently by viscous effects since  $Pm = 1$  here)

$$\gamma_{\max}^{\text{AMRI}} > \eta (k_{\max}^{\text{AMRI}})^2, \quad (16)$$

where  $k_{\max}^{\text{AMRI}} = m_{\max}^{\text{AMRI}} / s$  is the most unstable azimuthal wavenumber. Substituting Eqs. (14) and (15) in the relation above yields

$$Ha_\phi^2 > 2 \left(1 - \frac{q}{4}\right) Re \quad (17)$$

when considering  $\Omega \approx \Omega_a$ ,  $s \approx d$ , and  $Pm = 1$ .

For increasing field strengths, large azimuthal modes are stabilized by magnetic tension and the spectrum of unstable modes shifts toward lower  $m$ . The condition  $m_{\max}^{\text{AMRI}} \geq 1$  provides an upper limit on the field strength for instability which, for  $Pm = 1$  and using the same values for  $\Omega$  and  $s$  as above, reads

$$Ha_\phi \leq \left(q - \frac{q^2}{4}\right)^{1/2} Re. \quad (18)$$

Combining Eqs. (17) and (18), we obtain the instability condition

$$2 \left(1 - \frac{q}{4}\right) Re < Ha_\phi^2 \leq q \left(1 - \frac{q}{4}\right) Re^2 \quad (19)$$

when  $q < 4$ . For our simulations where  $q \approx 1$ , Eq. (19) reduces to

$$\frac{3}{2} Re < Ha_\phi^2 \leq \frac{3}{4} Re^2 \quad (20)$$

or equivalently

$$\sqrt{\frac{3}{2}} \frac{1}{Re^{1/2}} < Le_\phi \leq \frac{\sqrt{3}}{2} \quad (21)$$

since  $Ha_\phi = Le_\phi Re$  when  $Pm = 1$ . Another prediction from the local linear theory of Masada et al. (2006) that will be used in the following is the critical AMRI mode

$$m_{\text{crit}}^{\text{AMRI}} = (2q)^{1/2} \Omega / \omega_A. \quad (22)$$

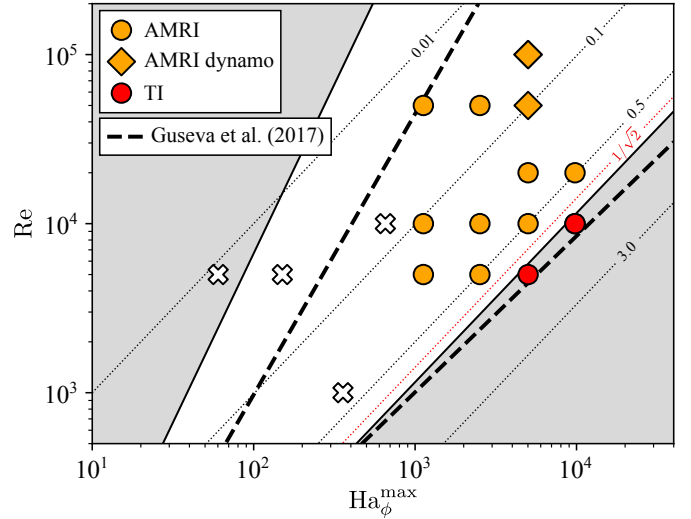


**Fig. 4.** Instability domain of the unstratified ( $N = 0$ ) axisymmetric solutions at  $Pm = 1$  and comparison with local and global linear stability analysis results. The Reynolds number  $Re$  is shown as a function of  $Ha_\phi^{\max}$ , the maximum azimuthal Hartmann number in the fluid domain at the perturbation time  $t_{\text{pert}}$ . Crosses denote stable runs, that is simulations where the applied nonaxisymmetric perturbations decay. Orange (red) symbols display runs where AMRI (TI) is identified. Circles (squares) denote transient (self-sustained) turbulence for the nonlinear instability evolution. The white area shows the region unstable to AMRI according to order of magnitude estimates based on a local linear analysis (Eq. (20)). AMRI is stabilized by diffusive effects at lower magnetic field strengths (gray area on the left) and by magnetic tension at larger field strengths (gray area on the right). The thin dotted lines are isocontours of the azimuthal Lehnert number  $Le_\phi^{\max} = Ha_\phi^{\max} / Re$ . For  $Le_\phi^{\max}$  up to  $1/\sqrt{2}$  (red dotted line) the expected maximum growth rate of AMRI is larger than the one of TI (Eq. (24)). The thick dashed lines are reproduced from Fig. 1a of Guseva et al. (2017b) and show the lower and upper neutral stability lines of AMRI from their global linear analysis of Taylor–Couette flow for a quasi-Keplerian shear.

As mentioned above, the axisymmetric solutions explored here are in principle unstable to both AMRI and TI. However, in the AMRI regime defined by Eq. (21), the expected most unstable TI mode is virtually always growing slower than the corresponding AMRI mode. The most unstable TI mode is  $m_{\max}^{\text{TI}} = 1$  and its adiabatic growth rate, in the presence of rotation, is  $\gamma_{\max}^{\text{TI}} \sim \omega_A^2 / \Omega$  (Pitts & Tayler 1985; Spruit 1999; Bonanno & Urpin 2013). AMRI dominates over TI when  $\gamma_{\max}^{\text{AMRI}} > \gamma_{\max}^{\text{TI}}$ , that is

$$\frac{\omega_A}{\Omega} < \left(\frac{q}{2}\right)^{1/2}. \quad (23)$$

When assuming  $\Omega \approx \Omega_a$ ,  $s \approx d$ , and  $q \approx 1$  as done above, this condition reads

$$Le_\phi < 1/\sqrt{2} \quad (24)$$

which is slightly smaller than the upper bound of Eq. (21). Similarly to what we obtain here using simple order of magnitude estimates, Jouve et al. (2015) showed that TI dominates over AMRI when  $Le_\phi \geq 1$  by applying a local linear dispersion relation to dominant azimuthal field configurations obtained from direct numerical simulations.

Figure 4 compares our numerical simulation results with the predictions from the local linear analysis just discussed. Crosses show runs where the applied nonaxisymmetric perturbations decay and no instability is found; for circles and squares,

the perturbations grow exponentially over time. Runs where, as demonstrated in the next section, we observe AMRI (orange symbols) fall within the region of the parameter space predicted by the instability condition Eq. (20) (white background) as expected. For low azimuthal field strengths  $(Ha_\phi^{\max})^2 < 3Re/2$  (gray background on the left) where AMRI is stabilized by diffusive effects according to the estimates above, we found no unstable run.

For larger azimuthal field strengths  $(Ha_\phi^{\max})^2 > 3Re^2/4$  (gray background on the right), AMRI is expected to be suppressed by magnetic tension and we indeed observe TI (red circles). Evidence of TI in these simulation runs is provided in Appendix A. The critical  $Le_\phi^{\max}$  of  $1/\sqrt{2}$  for which the maximum TI growth rate becomes larger than the one of AMRI (red dotted line; cf. Eq. (24)) lies close to the boundary where AMRI is suppressed. In other words, in the AMRI regime, the maximum TI growth rate is virtually always lower than the one of AMRI.

Guseva et al. (2017b) performed a global linear stability analysis of AMRI in Taylor–Couette flow with a quasi-Keplerian shear that resembles the one employed here. The lower and upper neutral instability lines calculated by the authors (thick dashed lines in Fig. 4) agree remarkably well with our numerical simulation results.

In the remainder of this work, we focus on the AMRI regime only. In Sect. 5 we discuss the nonlinear evolution of the instability but we anticipate here that transient AMRI turbulence (orange circles in Fig. 4) is generally observed and only two runs at  $Re \geq 5 \times 10^4$  show self-sustained turbulence (orange squares).

#### 4.2. Evidence of AMRI

We now analyze the linear evolution of the instability observed in our numerical simulations and provide evidence of AMRI. Here we focus on the run at  $Re = 5 \times 10^4$  and  $Ha_\phi^{\max} = 5012$  as an example. The perturbations are introduced at time  $t_{\text{pert}} = 326.0$ . Similar results are obtained for the other unstable runs of Fig. 4 and we therefore do not discuss them in detail here.

Figures 5a,b present the initial temporal evolution of the toroidal and poloidal magnetic energies of various azimuthal modes  $m$  in this run. The energies are calculated over the spherical surface at radius  $r/r_o = 0.9$  and map the outer fluid regions where the instability first develops (Fig. 6a). As expected for AMRI, the instability fluctuations are larger in the outer equatorial region where the unstable modes have higher growth rates due to the stronger background shear (Fig. 1a).

Nonaxisymmetric azimuthal modes  $m < 25$  grow exponentially typically after about 10 system rotations from the perturbation time until  $t - t_{\text{pert}} \approx 25$  (Figs. 5a,b). The background axisymmetric ( $m = 0$ ) azimuthal field (black line in Fig. 5a) slowly decays due to Ohmic diffusion and its evolution is practically stationary during the linear instability growth. We also observe the generation of an initially weak and decaying axisymmetric poloidal field (black line in Fig. 5b). This field is produced from weak nonlinear correlations of the initial flow and field instability fluctuations.

Figure 5c displays the growth rates of the nonaxisymmetric azimuthal modes  $m$  from 1 to 25, calculated from the evolution of the poloidal (dashed line) and toroidal (solid line) magnetic energies above during the period  $t - t_{\text{pert}} = 9 - 24$  of the linear instability growth. The two growth rates spectra are in good agreement between each other. According to the toroidal spectrum, modes  $m < 24$  are linearly unstable. The most unstable mode is  $m_{\text{max}} = 14$ , although very similar growth rates are observed for the two adjacent modes  $m = 13$  and 15. The lon-

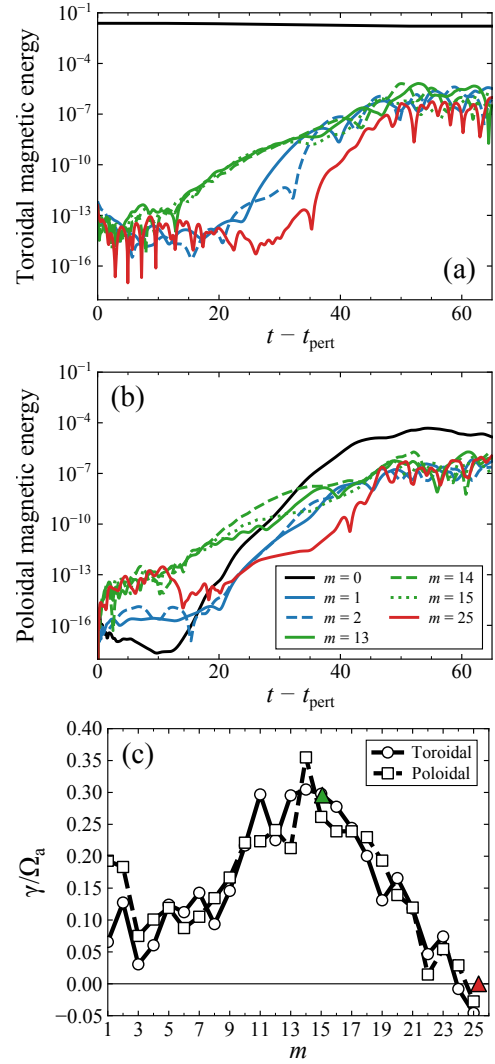


**Fig. 5.** Temporal evolution of various azimuthal modes and observed growth rates for the unstratified run at  $Re = 5 \times 10^4$ ,  $Ha_\phi^{\max} = 5012$ , and  $Pm = 1$ . (a) Toroidal and (b) poloidal magnetic energies of various linearly unstable azimuthal modes  $m$  as a function of time. The energies are calculated over the spherical surface at radius  $r/r_o = 0.9$ . The most unstable linear mode is  $m = 14$ . The first subcritical mode observed for both energy components is  $m = 25$ . (c) Linear growth rates  $\gamma/\Omega_a$  of the azimuthal modes  $1 \leq m \leq 25$ . The growth rates are calculated by fitting the toroidal (solid line) and poloidal (dashed line) magnetic energy evolution shown in (a,b) during the period  $t - t_{\text{pert}} = 9 - 24$ . The green and red triangles show, respectively, the most unstable and the critical AMRI modes predicted by the local linear theory and evaluated as explained in the main text.

gitudinal structure of the nonaxisymmetric azimuthal field  $B'_\phi$  is compatible with such dominant modes (Fig. 6b).

The observed most unstable mode  $m_{\text{max}}$  and its growth rate  $\gamma_{\text{max}}$  closely agree with the ones expected from the local linear theory discussed in the previous section. Equation (14) indeed provides  $\langle m_{\text{max}}^{\text{AMRI}} \rangle \approx 15$ , which is very close to the observed most unstable mode. Here and in the remainder of this section the angular brackets  $\langle \cdot \rangle$  denote average over a spherical surface at radius  $r/r_o = 0.9$  where the azimuthal modes spectra above are calculated. Based on Eq. (15), the expected maximum growth rate of AMRI is  $\langle \gamma_{\text{max}}^{\text{AMRI}} \rangle / \Omega_a \approx 0.29$ , which also closely agrees with the one observed from the toroidal spectrum at 0.30 (Fig. 5c).



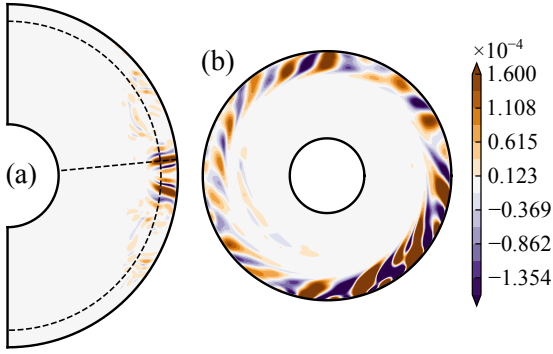


**Fig. 6.** Snapshot of the nonaxisymmetric azimuthal field  $B'_\phi$  during the linear growth of the instability ( $t-t_{\text{pert}} = 22$ ) for the run in Fig. 5. (a) Meridional cut at longitude  $\phi = 90^\circ$ . The curved dashed line shows radius  $r/r_o = 0.9$  where the magnetic energies of Figs. 5a,b are calculated. (b) Azimuthal cut at colatitude  $\theta = 85^\circ$  passing through a local maximum of  $B'_\phi$  (shown as an oblique dashed line in (a)).

The toroidal spectrum in Fig. 5c shows that the azimuthal modes  $m \geq 24$  are initially subcritical. This is again compatible with the local linear theory which predicts a critical azimuthal mode  $\langle m_{\text{crit}}^{\text{AMRI}} \rangle \approx 25$  (Eq. (22); red triangle in Fig. 5c). The linearly stable modes start to grow only at  $t-t_{\text{pert}} \gtrsim 25$  due to nonlinear mode energy transfers (the red line in Figs. 5a,b displays the evolution of  $m = 25$  as an example), when we verified that the axisymmetric magnetic energy becomes comparable in amplitude to the nonaxisymmetric one. The nonlinear growth rates of the modes  $m = 1$  and  $m = 2$  (blue lines in Figs. 5a,b) are roughly twice the growth rate of  $m_{\text{max}}$ , possibly because of mode interactions between the faster growing linear modes. Finally, the instability saturates at  $t-t_{\text{pert}} \approx 55$  with the nonaxisymmetric poloidal and toroidal energies roughly in equipartition.

Figure 7 displays the observed maximum growth rates  $\gamma_{\text{max}}$  and the most unstable azimuthal modes  $m_{\text{max}}$  for some of the unstable runs of Fig. 4 in the AMRI regime. The simulation data points are shown as a function of  $\langle \omega_A/\Omega \rangle$  at the perturbation time. The numerical results are in good agreement with the local linear analysis predictions for AMRI (Eqs. (15) and (14)), which are indicated by the gray shaded regions. The largest differences between the numerical and theoretical values are of about 20% in the maximum growth rate and of a factor 2 in the most unstable mode. Such differences are surprisingly very limited considering all the simplifying assumptions of the local linear analysis, which can only roughly describe the global modes excited in our numerical simulations.

## 5. Nonlinear solutions

In this section we discuss the nonlinear evolution of AMRI and describe the turbulent solutions obtained for unstratified and stratified flows. First, we consider the unstratified runs at  $\text{Pm} = 1$  of the previous section. In Sect. 5.1 we describe in detail the fiducial dynamo run at  $\text{Re} = 5 \times 10^4$  and  $\text{Ha}_\phi^{\text{max}} = 5012$  and we examine the dynamo onset in Sect. 5.2. The effect of  $\text{Pm}$  on the dynamo onset is presented in Sect. 5.3. Finally, Sect. 5.4 analyzes the nonlinear solutions obtained when including stable stratification.

### 5.1. Fiducial dynamo run

We describe the self-sustained turbulent solution of run U0 at  $\mathcal{N} = 0$ ,  $\text{Re} = 5 \times 10^4$ ,  $\text{Pm} = 1$ , and  $\text{Ha}_\phi^{\text{max}} = 5012$ , which we

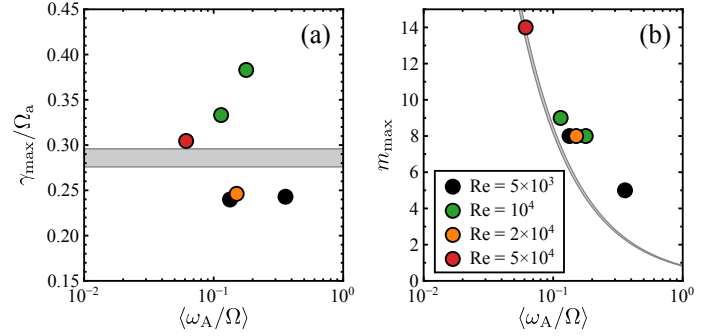


**Fig. 7.** Comparison of the observed most unstable AMRI modes and their growth rates with the local linear theory predictions. (a) Maximum growth rates  $\gamma_{\text{max}}$  and (b) most unstable azimuthal modes  $m_{\text{max}}$  as a function of  $\langle \omega_A/\Omega \rangle$ . The AMRI runs shown are those of Fig. 4 at  $(\text{Re}, \text{Ha}_\phi^{\text{max}}) = (5 \times 10^3, 1125), (5 \times 10^3, 2520), (10^4, 1125), (10^4, 2520), (2 \times 10^4, 5012),$  and  $(5 \times 10^4, 5012)$ . For each run,  $\gamma_{\text{max}}$  and  $m_{\text{max}}$  are calculated from the evolution of the toroidal magnetic energy of the linearly unstable modes as explained in the main text. The gray shaded regions display the range of maximum growth rates and most unstable modes predicted by the local linear theory for these runs.

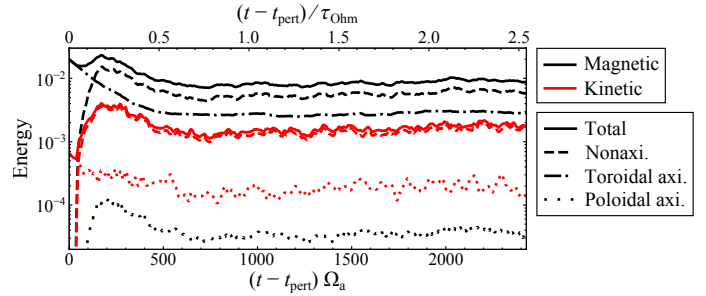


**Fig. 8.** Temporal evolution of the kinetic (red lines) and magnetic (black lines) energies for the fiducial dynamo run U0 ( $\mathcal{N} = 0$ ,  $\text{Re} = 5 \times 10^4$ ,  $\text{Pm} = 1$ , and  $\text{Ha}_\phi^{\text{max}} = 5012$ ). The axisymmetric toroidal kinetic energy of the forced azimuthal flow is the dominant energy contribution (not shown) and has been subtracted from the calculation of the total kinetic energy. The lower (upper) horizontal axis shows time scaled in units of the rotation timescale  $\tau_\Omega = 1/\Omega_a$  (Ohmic diffusion time  $\tau_{\text{Ohm}}$ ).

refer to as the fiducial dynamo run hereafter. The linear phase of the instability growth in this run has been discussed in Sect. 4.2.

Figure 8 presents the temporal evolution of the various components of the kinetic and magnetic energies. The dominant (stationary) toroidal axisymmetric kinetic energy of the background flow is  $\frac{1}{2} \int \bar{u}_\phi dV \approx \frac{1}{2} \int u_f dV \approx 2.3$  (not shown) and has been subtracted from the total kinetic energy contribution. After around 700 system rotations from the perturbation time  $t_{\text{pert}} = 326.0$ , a stationary regime is reached. The magnetic energy of this state is dominantly nonaxisymmetric (dashed black line). The axisymmetric toroidal magnetic energy (dot dashed black line) is the second largest contribution, with an amplitude about 3 times smaller than the total magnetic energy. The axisymmetric poloidal field  $\bar{B}_p$ , generated by the instability fluctuations through the azimuthal component of the mean electromotive force (EMF)  $\bar{\mathcal{E}} = \bar{\mathbf{u}}' \times \bar{\mathbf{B}}'$ , is decisively weaker and saturates at an energy (dotted black line) roughly 2 orders of magnitude lower than the one of the axisymmetric toroidal field. Although weak, a positive EMF feedback on  $\bar{B}_p$  as the one observed here is crucial for MRI dynamos to operate. The  $\Omega$ -effect obtained by shearing this weak  $\bar{B}_p$  through the background differential rotation provides indeed the required closure for self-sustained

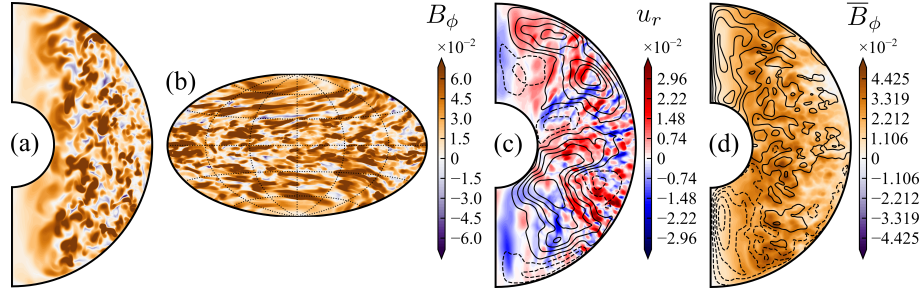


**Fig. 9.** Steady flow and magnetic field solution of the fiducial dynamo run U0 at time  $t_s = 1241$  (or  $t_s - t_{\text{pert}} = 915$ ). (a,b) Meridional cut and surface projection at  $r/r_0 = 0.8$  of the azimuthal field  $B_\phi$ . (c,d) Meridional cuts of the radial flow velocity  $u_r$  and of the axisymmetric azimuthal field  $\bar{B}_\phi$ . Black isocontours in (c) and (d) show the meridional circulation and the axisymmetric poloidal field respectively.

dynamo action (Rincon et al. 2007; Rincon 2019). The time averaged nonaxisymmetric magnetic energy of the steady state is about 4 times larger than the kinetic one (dashed red line). Similar turbulent magnetic to kinetic energy ratios are observed in global and local simulations of MRI turbulence with zero net flux (Reboul-Salze et al. 2021).

Figure 9 illustrates the complex turbulent character of the solution in the steady state. The magnetic field is small scaled in the meridional directions, while it presents elongated structures in the azimuthal direction, which are typical of MRI turbulence and are due to shear effects (Figs. 9a,b). Inside the tangent cylinder, the imaginary vertical cylindrical surface tangent to the inner boundary at the equator, the magnetic field is weak since AMRI is less active due to the low background shear (Fig. 1). Nonetheless, these regions host large scale axisymmetric poloidal fields confined at high latitudes by the meridional flow (black isocontours in Figs. 9c,d). Outside the tangent cylinder, both  $\bar{B}_p$  and  $\bar{B}_\phi$  are concentrated in small flux patches generated by the instability fluctuations (Fig. 9d). The structures of the flow velocity components are similar to those of the magnetic field, except for  $u_r$  where the large scale meridional circulation produces radial plumes (Fig. 9c).

Dynamo action occurs when the magnetic field is sustained for a period longer than its characteristic Ohmic diffusion time  $\tau_{\text{Ohm}} = l_B^2/\eta$ , where  $l_B$  is a characteristic magnetic field length scale. Since the typical radial and latitudinal length scales of the magnetic field in the stationary state are similar, we estimate  $l_B$  based on the horizontal length scales only. To this end, we define the instantaneous horizontal half wavelength of the field

$$l_{B,\perp} = \frac{\pi d}{\ell_B}, \quad (25)$$

where

$$\ell_B = \frac{\sum_{\ell,m} \ell \langle B_{\ell,m}^2 \rangle}{\langle B^2 \rangle} \quad (26)$$

is the mean SH degree of the field (Christensen & Aubert 2006). Here  $B_{\ell,m}$  is the coefficient at degree  $\ell$  and order  $m$  of the SH expansion of the field and the angular brackets denote a volume integral over the fluid domain. The time average of  $l_{B,\perp}$  during the steady state of the fiducial dynamo run is  $\hat{l}_{B,\perp} = 0.14 d$ , which yields an Ohmic diffusion time  $\tau_{\text{Ohm}} \approx 955 \Omega_a^{-1}$ . The top horizontal axis of Fig. 8 shows that the quasi steady evolution of this run, which we define to start after about  $670 \Omega_a^{-1}$  from the perturbation time, covers  $1.84 \tau_{\text{Ohm}}$  and therefore self-sustained dynamo action is at work.

Hereafter we classify a simulation run as a dynamo if its quasi steady evolution lasts longer than  $\tau_{\text{Ohm}}$ . The simulation run presented here is the first MRI dynamo at a value of the magnetic Prandtl number  $\text{Pm}$  as low as 1 ever reported in a global setup. Previous global numerical studies have shown self-sustained MRI turbulence only for  $\text{Pm} \geq 10$  (Guseva et al. 2017b; Reboul-Salze et al. 2021). We remind here that these solutions have to be interpreted as small-scale dynamos, in the sense that the generated flow and magnetic fields are at scales smaller than the forcing scale of the background flow, which is on the order of  $r_0$  in our runs (e.g., Rincon 2019).

Similarly to the above, we define the horizontal half wavelength of the flow  $l_{u,\perp} = \pi d/\ell_u$ , where  $\ell_u$  is the mean SH degree of  $|\mathbf{u} - \mathbf{u}_r|$ , the flow velocity amplitude after subtracting the contribution of the forcing. For the simplicity of notation, we refer to  $l_{u,\perp}$  and  $l_{B,\perp}$  as their time averaged values over a period of stationary evolution of the solution hereafter. For run U0,  $l_{u,\perp} = 0.19 d$ , which is slightly larger than  $l_{B,\perp}$ . These horizontal length scales are listed, together with the control parameters and other output measures, in Table 1 for run U0 and for the other unstratified dynamos and stratified runs that we shall discuss in the next sections.

## 5.2. Dynamo onset at $\text{Pm} = 1$

Dynamo action driven by MRI is an inherently nonlinear phenomenon: it requires instability fluctuations that transiently grow to finite amplitudes, leading to nonlinear effects that eventually sustain the turbulence (Rincon et al. 2008). Linear MRI modes can easily reach finite amplitudes since they exhibit nonmodal growth, that is they can transiently grow faster than the least stable eigenmode on short timescales (e.g., Balbus & Hawley 1992; Squire & Bhattacharjee 2014; Mamatsashvili et al. 2020). Nonmodal effects are a well known property of non-self-adjoint linear systems, which include not only those prone to MRI but also purely hydrodynamical shear flows (Schmid 2007).

As a consequence of their nonmodal character, the excitation of MRI dynamos strongly depends on the amplitude and morphology of the initial condition (Riols et al. 2013; Guseva et al. 2017a). Consistently with these findings, as anticipated in Sect. 4.1, we observe self-sustained dynamo action in our unstratified simulations at  $\text{Pm} = 1$  and fixed  $\text{Re}$  only when the field strength of the perturbed axisymmetric solution is large enough. Figure 10a compares the temporal evolution of the magnetic energy  $E_{\text{mag}}$ , scaled as in Sect. 3, of the fiducial dynamo run U0 (solid black line) with two runs at lower  $\text{Ha}_\phi^{\text{max}}$ . The latter runs show transient turbulence where the instability decays after saturating for a period which shortens when  $\text{Ha}_\phi^{\text{max}}$  decreases.

**Table 1.** Input parameters and output diagnostics of the unstratified ( $N = 0$ ) dynamo runs and of the stratified ( $N > 0$ ) runs.

Name	$\mathcal{N}$	$Re/10^4$	Pm	$Ha_\phi^{\max}$	Pr	$t_{\text{pert}}$	$l_c/d$	Regime	$Rm_{\text{eff}}$	$\tau_{\text{eddy}}/\tau_\Omega$	$\tau_{\text{Ohm}}/\tau_\Omega$	$\Delta t/\tau_{\text{Ohm}}$	$l_{u,\perp}/d$	$l_{B,\perp}/d$	$l'_{u,\perp}/d$	$l'_{B,\perp}/d$
U0	0	5	1	5012	–	326	–	D	823	5.8	955	1.84	0.190	0.138	0.090	0.075
U1	0	5	2	5012	–	566	–	D	2136	3.3	828	0.82	0.142	0.091	0.067	0.057
U2	0	10	1	5012	–	654	–	D	2527	2.2	956	1.07	0.114	0.098	0.054	0.059
U3	0	10	0.6	5012	–	412	–	D	1035	4.2	935	1.60	0.144	0.125	0.068	0.067
S0	1	5	1	–	$10^{-3}$	–	0.141	T	677	6.3	1206	0.95	0.169	0.155	0.083	0.076
S1	1	5	1	–	$10^{-2}$	–	0.045	T	669	6.4	1878	0.40	0.169	0.194	0.084	0.084
S2	1	5	1	–	$10^{-1}$	–	0.014	T	770	6.7	2946	0.17	0.204	0.243	0.102	0.083
S3	10	5	1	–	$10^{-4}$	–	0.141	T	490	9.3	2052	0.37	0.173	0.203	0.086	0.083
S4	10	5	1	–	$10^{-3}$	–	0.045	T	424	13.0	9831	0.19	0.216	0.443	0.107	0.091
S5	10	5	1	–	$2 \times 10^{-3}$	–	0.032	T	438	13.6	17912	0.09	0.238	0.599	0.117	0.103
S6	10	5	1	–	$10^{-2}$	–	0.014	S	–	–	–	–	–	–	–	–
S7	20	5	1	–	$10^{-4}$	–	0.100	T	415	12.5	4076	0.17	0.197	0.286	0.098	0.087
S8	20	5	1	–	$5 \times 10^{-4}$	–	0.045	T	373	17.1	18273	0.05	0.254	0.605	0.125	0.110
S9	20	5	1	–	$10^{-3}$	–	0.032	T	429	15.6	29011	0.04	0.265	0.762	0.131	0.121
S10	20	5	1	–	$5 \times 10^{-3}$	–	0.014	S	–	–	–	–	–	–	–	–

**Notes.** The Reynolds number, the magnetic Prandtl number, and the Prandtl number are Re, Pm, and Pr respectively.  $Ha_\phi^{\max}$  is the maximum value of the azimuthal Hartmann number in the fluid domain at the perturbation time  $t_{\text{pert}}$ . The initial condition of the stratified runs is the solution of fiducial dynamo run U0 at time  $t_s = 1241$  (Fig. 9).  $l_c/d$  is the critical radial flow length scale below which thermal diffusion is expected to weaken the stabilizing buoyancy. As for the run regime, D, T, and S stand for dynamo, transient turbulence, and stable respectively.  $Rm_{\text{eff}}$  is the effective magnetic Reynolds number based on the rms flow velocity after subtracting the forced azimuthal flow.  $\tau_{\text{eddy}}$  and  $\tau_{\text{Ohm}}$  are the eddy turnover time and the Ohmic diffusion time respectively and are reported in units of the rotation timescale  $\tau_\Omega = 1/\Omega_a$ .  $\Delta t$  is the period of quasi steady evolution and over which all time averages are calculated. The horizontal length scales based on the (turbulent) flow velocity and magnetic field are ( $l'_{u,\perp}$  and  $l'_{B,\perp}$ )  $l_{u,\perp}$  and  $l_{B,\perp}$  respectively. See the main text for definitions of all these output diagnostics.

The turbulent magnetic Reynolds number

$$Rm' = \frac{u'_{\text{rms}} d}{\eta} \quad (27)$$

and the turbulent Lundquist number

$$Lu' = \frac{B'_{\text{rms}} d}{(\mu_0 \rho)^{1/2} \eta}, \quad (28)$$

where  $u'_{\text{rms}}$  and  $B'_{\text{rms}}$  are the root mean square (rms) nonaxisymmetric flow and magnetic field strengths respectively, can be used to compare the amplitudes of the flow and field instability fluctuations between these runs. The peak values reached by  $Rm'$  and  $Lu'$  increase with  $Ha_\phi^{\max}$  (Figs. 10c,e), arguably producing a stronger mean EMF  $\bar{\mathcal{E}}$  which sustains the axisymmetric field against resistive effects at the larger  $Ha_\phi^{\max}$  of 5012 of run U0. As already mentioned above, this instability-driven EMF is key to generate the axisymmetric poloidal field required for MRI dynamos to operate. We note that studies of AMRI in Taylor–Couette flow also show that both the turbulent flow and field amplitudes increase with the imposed background field strength as we observe here (Rüdiger et al. 2013).

As anticipated in Sect. 4.1, we find dynamo action for  $Re \geq 5 \times 10^4$ , that is when the azimuthal flow forcing is strong enough. Figure 10b indeed demonstrates that  $E_{\text{mag}}$  in runs at a fixed  $Ha_\phi^{\max}$  of 5012 decays for  $Re \leq 2 \times 10^4$ , while a quasi steady state is reached in the two other runs at larger Re. The peak amplitudes of  $Rm'$  and  $Lu'$  increase with the Reynolds number (Figs. 10d,f), which again suggests that dynamo action occurs when the mean EMF becomes strong enough. The background differential rotation contrast from pole to equator  $\Delta\Omega$  scales roughly as  $Re/2$  (Sect. 2). This produces a stronger  $\Omega$ -effect in the two runs at larger Re which also helps to sustain the axisymmetric azimuthal field  $\bar{B}_\phi$ .

We remark here that the perturbed axisymmetric azimuthal field solutions of these runs at fixed  $Ha_\phi^{\max}$  are very similar but not

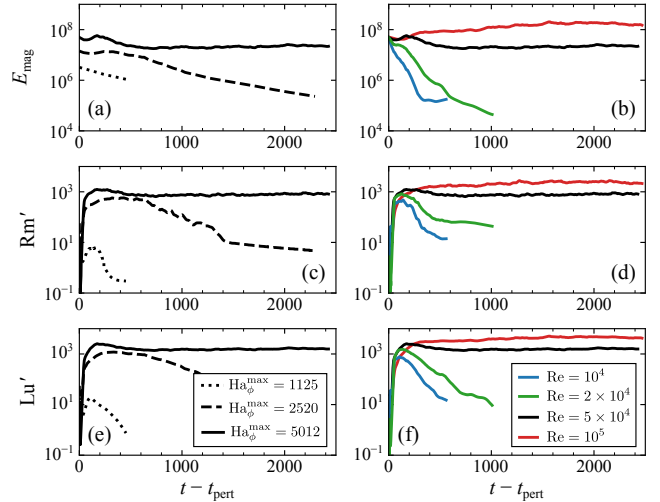


**Fig. 10.** Temporal evolution of the (a,b) magnetic energy  $E_{\text{mag}}$ , the (c,d) turbulent magnetic Reynolds number  $Rm'$ , and the (e,f) turbulent Lundquist number  $Lu'$  for six unstratified runs at  $Pm = 1$ . The solid black line shows the fiducial dynamo run U0. The left (right) panels present runs at  $Re = 5 \times 10^4$  ( $Ha_\phi^{\max} = 5012$ ) and different  $Ha_\phi^{\max}$  (Re) as indicated in the legend of the bottom panel.

exactly identical. Although mild, these differences may contribute to explain the regime change from decaying to self-sustained turbulence when increasing Re. The critical magnetic Reynolds number for the onset of MRI dynamo action indeed strongly depends on the initial condition itself (Riols et al. 2013).

### 5.3. Dependence of the dynamo onset on Pm

Local shearing box simulations with zero or nonzero net magnetic fluxes show that viscous and resistive effects strongly

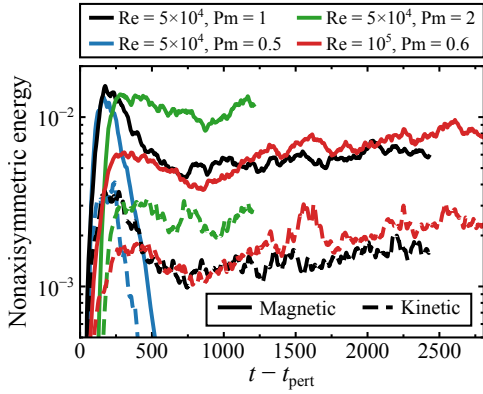


**Fig. 11.** Temporal evolution of the nonaxisymmetric kinetic (dashed lines) and magnetic (solid lines) energies for four unstratified runs at  $\text{Re} = 5 \times 10^4$  and  $\text{Re} = 10^5$  and different values of  $\text{Pm}$  as indicated in the legend at the top. The black lines show the fiducial dynamo run U0.

affect the saturated state of MRI turbulence (Lesur & Longaretti 2007; Fromang et al. 2007; Simon & Hawley 2009). In particular, magnetic diffusion limits the turbulence saturation level such that, at fixed  $\text{Re}$ , dynamo action is lost below a critical value of  $\text{Pm}$ , a behavior that we also find here.

Figure 11 presents the temporal evolution of the nonaxisymmetric kinetic and magnetic energies in run U0 (black lines) and in two other runs at the same  $\text{Re}$  of  $5 \times 10^4$ , but with  $\text{Pm} = 0.5$  and 2 (run U1) (green lines). After a few hundreds of system rotations, run U1 (green lines) reaches a quasi steady state covering a period  $\Delta t = 0.82 \tau_{\text{Ohm}}$  (Table 1). Given that the various energy components are stationary and that the period of quasi steady evolution is close to one Ohmic diffusion time, we consider this run as a dynamo. The time averaged turbulent kinetic and magnetic energies in the quasi steady state increase by about a factor 2 relative to run U0, in qualitative agreement with the shearing box studies mentioned above.

When decreasing  $\text{Pm}$  to 0.5, AMRI turbulence is maintained only for some tens of system rotations and then it decays away (blue lines in Fig. 11). We note that the perturbed axisymmetric azimuthal field configurations of these runs are different, but their mean strength increases when  $\text{Pm}$  lowers which, in principle, favors dynamo action as discussed in the previous section. While this cannot justify the observed dynamo behavior, it may explain the large peak values of the turbulent energies reached by the nondynamo run at  $\text{Pm} = 0.5$ , which are comparable to those of runs U0 and U1.

The shearing box MRI studies mentioned above also indicate that the critical  $\text{Pm}$  for dynamo onset decreases when  $\text{Re}$  increases (e.g., Fromang et al. 2007). At the largest  $\text{Re}$  of  $10^5$  that we explored here, we indeed observe dynamo action for a value of  $\text{Pm}$  as low as 0.6 (run U3; red lines in Fig. 11). After an initial transient of about 340 system rotations the turbulence reaches a quasi steady evolution lasting for  $1.6 \tau_{\text{Ohm}}$ . MRI dynamos at  $\text{Pm} < 1$  are reported in local shearing box simulations with net magnetic fluxes (Simon & Hawley 2009; Käpylä & Korpi 2011), but never so far in global setups as the one explored here.

#### 5.4. Effect of stable stratification on AMRI turbulence

We now study how stable stratification modifies unstratified AMRI turbulence at  $\text{Re} = 5 \times 10^4$  and  $\text{Pm} = 1$ . To this end, we solve Eqs. (2)–(4) using as initial condition the quasi steady solution of the fiducial dynamo run U0 at time  $t_s = 1241$  (Fig. 9).

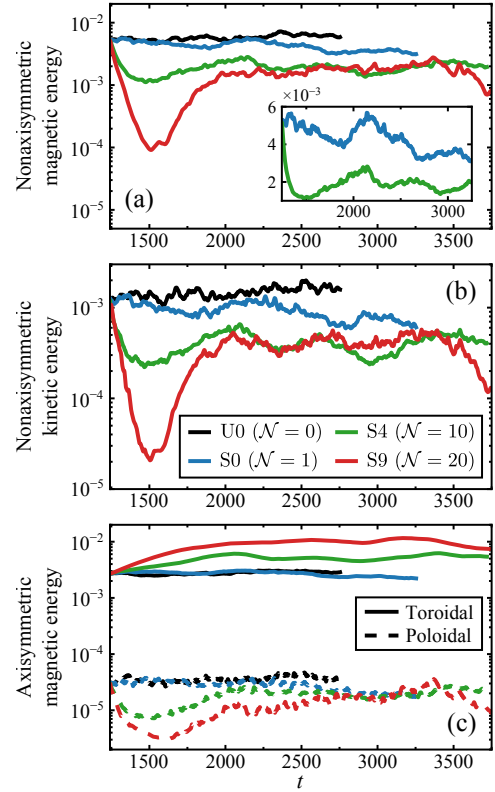


**Fig. 12.** Temporal evolution of the magnetic and kinetic energies of four unstratified and stratified runs at  $\text{Re} = 5 \times 10^4$  and  $\text{Pm} = 1$ . (a) Non-axisymmetric magnetic energy, (b) nonaxisymmetric kinetic energy, (c) axisymmetric toroidal (solid lines) and poloidal (dashed lines) magnetic energies as a function of time for the unstratified fiducial dynamo run U0 (black) and the three runs S0 ( $\mathcal{N} = 1$ ), S4 ( $\mathcal{N} = 10$ ), and S9 ( $\mathcal{N} = 20$ ) respectively (see the legend in the middle panel). All the stratified runs are at  $\text{Pr} = 10^{-3}$ . The inset in (a) shows the nonaxisymmetric magnetic energies of runs S0 and S4 on a linear scale. The initial condition of the stratified runs is the steady state solution of run U0 at time  $t_s = 1241$  shown in Fig. 9.

We first discuss the effect of stable stratification by varying  $\mathcal{N}$  at a fixed Prandtl number  $\text{Pr}$  of  $10^{-3}$ . Stable stratification strongly limits radial motions, modifying the characteristics of the turbulence. Figures 12a,b present the temporal evolution, starting at  $t = t_s$ , of the turbulent (nonaxisymmetric) magnetic and kinetic energies in run U0 (black lines) and in the three stratified runs S0 ( $\mathcal{N} = 1$ ), S4 ( $\mathcal{N} = 10$ ), and S9 ( $\mathcal{N} = 20$ ), showing that they lower when increasing stratification. After an initial transient which gets longer when increasing  $\mathcal{N}$ , the quasi steady evolutions of runs S4 (green lines) and S9 (red lines) cover  $0.95$  and  $0.19 \tau_{\text{Ohm}}$  respectively. The turbulence in the weakly stratified run S0 (blue lines) slowly decays following the resistive decay of the background axisymmetric field (blue lines in Fig. 12c). By limiting radial motions, stable stratification lowers the effective magnetic Reynolds number  $\text{Rm}_{\text{eff}} = u_{\text{rms}} d / \eta$  below the critical value for dynamo onset, which is of about 820 based on the unstratified simulations (Table 1). Here  $u_{\text{rms}} = \left( V^{-1} \int |\mathbf{u} - \mathbf{u}_f|^2 dV \right)^{1/2}$  is the rms flow velocity after subtracting the forced azimuthal flow. The energies of all stratified runs explored here display an oscillatory behavior (see the inset in Fig. 12a) which is characteristic of stratified MRI turbulence and is often attributed to an  $\alpha\Omega$ -dynamo process (Gressel 2010; Reboul-Salze et al. 2022).

The location and structure of the turbulence also change with stratification. The snapshots of  $B'_\phi$  in Figs. 13d–f reveal that

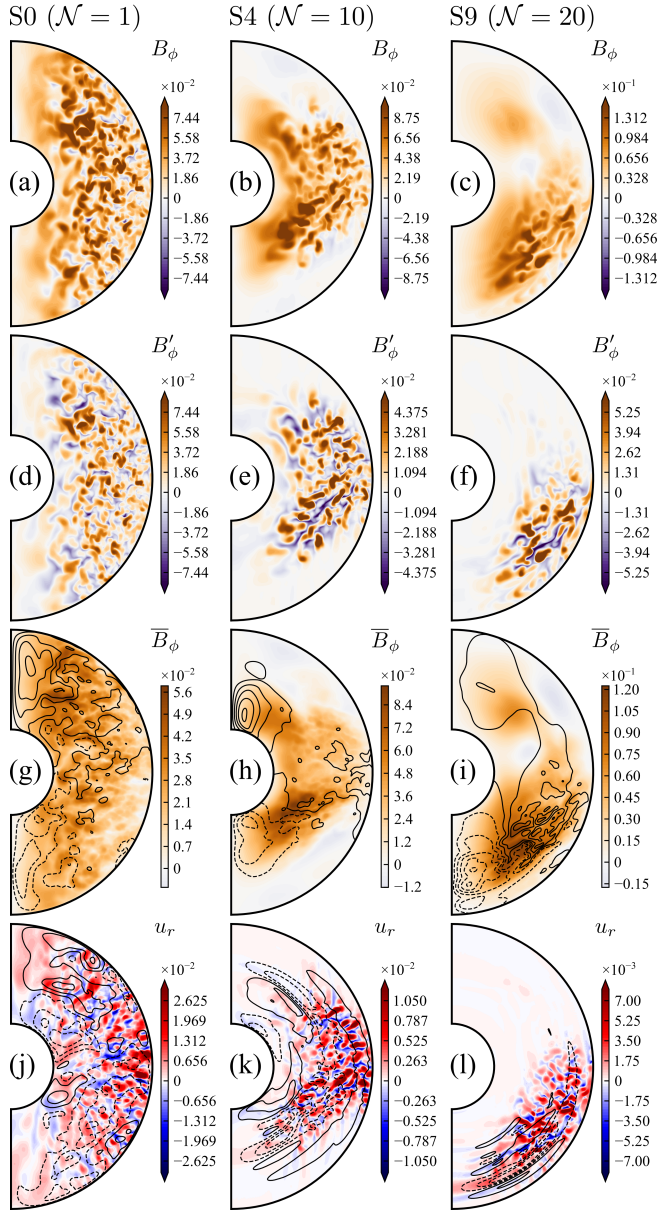


**Fig. 13.** Snapshots of the flow and magnetic field solutions of runs S0, S4, and S9 shown in Fig. 12. From top to bottom: meridional cuts of the azimuthal field  $B_\phi$ , nonaxisymmetric azimuthal field  $B'_\phi$ , axisymmetric azimuthal field  $\bar{B}_\phi$ , and radial flow velocity  $u_r$ . Black isocontours superimposed on  $\bar{B}_\phi$  and  $u_r$  show the axisymmetric poloidal field and the meridional circulation respectively.

the turbulence in the weakly stratified run S0 remains homogeneous outside the tangent cylinder as in the unstratified fiducial dynamo, while the instability is confined up to intermediate latitudes in run S4 and is almost entirely located in the southern hemisphere in the most stratified run S9. The unstable regions in the two latter runs correlate with the locations where the axisymmetric azimuthal field  $\bar{B}_\phi$  is stronger (Figs. 13h,i) and unstable to AMRI according to the local linear analysis, which predicts  $5.5 \times 10^{-3} < \bar{B}_\phi \leq 0.87$  based on the instability condition Eq. (21). Outside these locations,  $\bar{B}_\phi$  is too weak, with typical absolute amplitudes of  $10^{-3}$  or smaller, and AMRI modes are damped by diffusive effects.

In the most stratified run S9, the turbulence becomes weakly anisotropic, with structures elongated in the latitudinal direction

as expected (Fig. 13f). The horizontal turbulent field length scale  $l'_{B,\perp}/d$  is 0.12 in this run, which is 60% larger than the value of the weakly stratified run S0 (Table 1). In the latitudinal direction, the structures of the flow are less stretched than those of the field, as evidenced by comparing the snapshots of  $B_\phi$  (Fig. 13c) and  $u_r$  (Fig. 13l). The horizontal field length scale  $l_{B,\perp}/d$  is indeed as large as 0.76, whereas the one of the flow is lower at  $l_{u,\perp}/d = 0.27$ .

It is interesting to note that the axisymmetric toroidal magnetic energy increases with stratification (solid lines in Fig. 12c). This energy contribution dominates over the nonaxisymmetric one for  $N > 1$ , so that  $B_\phi$  is characterized by larger spatial scales as stratification increases (Figs. 13a–c). On the contrary, the axisymmetric poloidal magnetic energy weakly lowers with stratification (dashed lines in Fig. 12c). As a consequence, the ratio  $\bar{B}_{\phi,\text{rms}}/\bar{B}_{p,\text{rms}}$ , where  $\bar{B}_{\phi,\text{rms}}$  ( $\bar{B}_{p,\text{rms}}$ ) is the time averaged rms axisymmetric azimuthal (poloidal) field, increases when increasing  $N$  and ranges between 10 and 25 in our stratified simulations (Table 2). In the mean induction equation, the source terms that generate the axisymmetric toroidal field  $\bar{B}_\phi$  are the radial mean EMF  $\bar{\mathcal{E}}_r$  and the term associated to the  $\Omega$ -effect,  $s(\bar{\mathbf{B}}_p \cdot \nabla)\Omega$ , where  $\bar{\mathbf{B}}_p$  is the axisymmetric poloidal field. In runs S4 and S9,  $\bar{B}_\phi$  is mostly concentrated in large flux patches located where the turbulence is most active which suggests a positive feedback of  $\bar{\mathcal{E}}_r$  on its generation. The more coherent structure of the turbulence obtained when increasing stratification may yield locally stronger  $\bar{\mathcal{E}}_r$ , which then causes the observed increase in  $\bar{B}_\phi$ . Although  $\bar{B}_p$  is weak in all runs explored, the  $\Omega$ -effect – a key ingredient of MRI dynamos as mentioned before – is still of leading order due to the strong background shear. The positive feedback of the  $\Omega$ -effect on the generation of  $\bar{B}_\phi$  is suggested, for example, by the positive flux patch in the northern hemisphere observed in run S9 (Fig. 13i). The maximum of this flux patch is indeed located where  $\bar{B}_p$  (black isocontours in Fig. 13i) is roughly antiparallel to the shear direction  $\hat{e}_s$  as expected.

The ratio of the time averaged rms azimuthal field to the radial one  $B_{\phi,\text{rms}}/B_{r,\text{rms}}$  ranges between 3 and 5 in the unstratified and weakly stratified runs at  $N = 1$  and increases when stable stratification strengthens. At  $\text{Pr} = 10^{-3}$ , for example,  $B_{\phi,\text{rms}}/B_{r,\text{rms}}$  grows from 4.1 to 14.8 when increasing  $N$  from 1 to 20. This field ratio is in the range 2–6 in global compressible simulations of stratified MRI turbulence in accretion disks (Hawley et al. 2011, 2013), while local shearing box simulations obtain values around 2 (Shi et al. 2010).

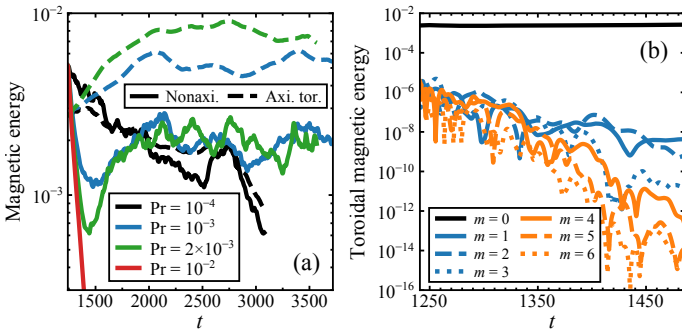
By reducing the amplitude of the temperature fluctuations, thermal diffusion can weaken the stabilizing buoyancy force in Eq. (2). This occurs when thermal diffusion acts faster than the buoyancy force, that is when  $\tau_\kappa < \tau_N$ , where  $\tau_\kappa = l_r^2/\kappa$  is the thermal diffusion timescale at the radial flow length scale  $l_r$  and  $\tau_N = 1/N$  is the buoyancy timescale. By equating these two timescales, we obtain the critical (radial) flow length scale  $l_c = (\kappa/N)^{1/2}$ , or  $l_c/d = (\text{Pr Re } N)^{-1/2}$ , below which thermal diffusion weakens buoyancy. To explore the effect of thermal diffusion in our stratified simulations at  $\text{Re} = 5 \times 10^4$  and  $\text{Pm} = 1$ , we varied the Prandtl number  $\text{Pr}$  at fixed  $N$ .

Figure 14a displays the temporal evolution of the turbulent magnetic energy (solid lines) in four runs at  $N = 10$  with  $\text{Pr}$  increasing from  $10^{-4}$  to  $10^{-2}$ . While AMRI is observed for  $\text{Pr} \leq 2 \times 10^{-3}$ , further increasing the Prandtl number to  $10^{-2}$  (solid red line) suppresses the instability. In this stable run the nonaxisymmetric modes decay at a rate increasing with the azimuthal wavenumber  $m$  as expected (Fig. 14b).

**Table 2.** Time averaged diagnostics for the flow, the magnetic field, and the angular momentum transport for all unstable runs of Table 1.

Name	$\mathcal{N}$	$\text{Re}/10^4$	Pm	Pr	$\overline{B}_{\phi,\text{rms}}}/\overline{B}_{p,\text{rms}}$	$B_{\phi,\text{rms}}/B_{r,\text{rms}}$	$u'_{\text{rms}}/10^{-3}$	$B'_{\text{rms}}/10^{-3}$	$\overline{u}_{M,\text{rms}}/10^{-3}$	$R$	$\tilde{\nu}_T \times 10^5$
U0	0	5	1	–	8.9	3.9	15.5	30.8	5.6	11.9	$37.1 \pm 4.5$
U1	0	5	2	–	7.4	3.3	20.3	42.2	6.7	13.0	$74.0 \pm 8.1$
U2	0	10	1	–	7.4	3.1	24.3	46.1	7.1	11.8	$88.4 \pm 7.7$
U3	0	10	0.6	–	9.0	3.6	16.5	30.5	5.2	10.4	$38.1 \pm 8.0$
S0	1	5	1	$10^{-3}$	9.6	4.1	13.1	28.0	3.5	11.1	$30.8 \pm 3.4$
S1	1	5	1	$10^{-2}$	10.2	3.9	13.2	26.5	2.0	9.4	$30.6 \pm 3.7$
S2	1	5	1	$10^{-1}$	12.2	4.7	15.3	28.5	2.0	6.8	$31.3 \pm 1.9$
S3	10	5	1	$10^{-4}$	10.9	4.4	9.6	22.1	1.9	10.1	$20.3 \pm 5.3$
S4	10	5	1	$10^{-3}$	16.2	6.9	8.4	18.3	1.3	6.6	$11.8 \pm 2.2$
S5	10	5	1	$2 \times 10^{-3}$	19.9	10.0	8.6	18.3	1.6	5.7	$8.2 \pm 1.1$
S7	20	5	1	$10^{-4}$	13.0	5.2	8.2	18.8	1.3	8.1	$14.3 \pm 4.3$
S8	20	5	1	$5 \times 10^{-4}$	20.3	10.9	7.3	16.2	1.4	6.2	$5.8 \pm 0.8$
S9	20	5	1	$10^{-3}$	24.6	14.8	8.5	17.6	1.5	5.2	$4.9 \pm 0.6$

**Notes.** The averages are evaluated over the periods  $\Delta t$  reported in Table 1.  $\overline{B}_{\phi,\text{rms}}}/\overline{B}_{p,\text{rms}}$  is the ratio of the rms axisymmetric azimuthal field to the rms axisymmetric poloidal field.  $B_{\phi,\text{rms}}/B_{r,\text{rms}}$  is the ratio of the rms azimuthal field to the rms radial field. The rms turbulent flow velocity and magnetic field are  $u'_{\text{rms}}$  and  $B'_{\text{rms}}$  respectively. The rms meridional flow velocity is  $\overline{u}_{M,\text{rms}}$ .  $R$  denotes the ratio of the volume averaged radial Maxwell stresses  $(\mu_0\rho)^{-1}\langle B'_r B'_\phi \rangle$  to the volume averaged radial Reynolds stresses  $\langle u'_r u'_\phi \rangle$ .  $\tilde{\nu}_T$  is the dimensionless turbulent viscosity estimated as explained in the main text; the error indicates 1 standard deviation in time.



**Fig. 14.** Effect of the Prandtl number  $\text{Pr}$  on the instability. (a) Nonaxisymmetric (solid lines) and axisymmetric toroidal (dashed lines) magnetic energies as a function of time in runs S3–S6 ( $\text{Re} = 5 \times 10^4$ ,  $\text{Pm} = 1$ ,  $\mathcal{N} = 10$ , and different values of  $\text{Pr}$  as indicated in the legend). Only the nonaxisymmetric energy is shown for run S6 at  $\text{Pr} = 10^{-2}$ . (b) Toroidal magnetic energy at radius  $r/r_o = 0.5$  as a function of time for the azimuthal modes  $m = 0$ –6 for the stable run S6.

The analysis of a few snapshots of the turbulent radial velocity  $u'_r$  shows that the radial flow length scale  $l_r$ , obtained from a volume average of  $u'_r / |\hat{\mathbf{e}}_r \cdot \nabla u'_r|$ , is  $\lesssim O(l_c)$  for  $\text{Pr} \leq 2 \times 10^{-3}$ , which suggests that buoyancy effects are limited by thermal diffusion in these runs. In the run at  $\text{Pr} = 10^{-2}$ , on the contrary,  $l_r/d \approx 0.05$  is several times larger than the critical length scale  $l_c/d = 0.014$ , hence thermal diffusion cannot reduce the effect of stable stratification, which is too strong and suppresses the instability. Similarly, we observe AMRI turbulence at  $\mathcal{N} = 20$  when  $\text{Pr} \leq 10^{-3}$ , whereas the instability is suppressed at the larger  $\text{Pr}$  of  $5 \times 10^{-3}$  (Table 1). A similar behavior where increasing buoyancy effects stabilizes the system is also typical of hydrodynamical shear instabilities in vertically stratified flow (Lignières et al. 1999). We remark here that strong enough latitudinal gradients of the differential rotation allow AMRI to develop even when  $l_c \ll l_r$  and thermal diffusion does not limit stable stratification (Joue et al. 2020).

Finally, we note that all stratified AMRI runs show either transient turbulence or cover periods too short to test for dynamo

action. For example, at  $\mathcal{N} = 10$ , we found decaying turbulence at  $\text{Pr} = 10^{-4}$  (Fig. 14a, solid black line). The decay rate of the turbulent fluctuations is compatible with the one of the axisymmetric azimuthal field which sustains the instability (Fig. 14a, dashed black line). In the two runs at  $\text{Pr} = 10^{-3}$  and  $2 \times 10^{-3}$ , the turbulence is sustained for 0.19 and 0.09 Ohmic diffusion times  $\tau_{\text{Ohm}}$  respectively and it may decay on longer timescales not captured here (Table 1). These periods correspond to, respectively, 140 and 115 eddy turnover times  $\tau_{\text{eddy}}$ , which ensure a robust statistics for the turbulence. Hereafter  $\tau_{\text{eddy}}$  is defined as the time averaged ratio  $l'_{u,\perp} / u'_{\text{rms}}$ .

## 6. Angular momentum transport

In this section we examine the transport of AM induced by AMRI in the unstratified and stratified simulations described above. An equation of conservation for the specific AM  $L = s \overline{u}_\phi = s^2 \overline{\Omega}$  can be obtained by averaging the azimuthal component of Eq. (2) over longitude and multiplying both members by  $s = r \sin \theta$ ,

$$\frac{\partial L}{\partial t} - s \mathbf{f} \cdot \hat{\mathbf{e}}_\phi = -\nabla \cdot (\mathbf{F}^{\text{MC}} + \mathbf{F}^{\text{RS}} + \mathbf{F}^{\text{VD}} + \mathbf{F}^{\text{MS}} + \mathbf{F}^{\text{MT}}), \quad (29)$$

where

$$\mathbf{F}^{\text{MC}} = \overline{u}_M L, \quad (30)$$

$$\mathbf{F}^{\text{RS}} = s \overline{u'_r u'_\phi} \hat{\mathbf{e}}_r + s \overline{u'_\theta u'_\phi} \hat{\mathbf{e}}_\theta, \quad (31)$$

$$\mathbf{F}^{\text{VD}} = -\frac{1}{\text{Re}} s^2 \nabla \overline{\Omega}, \quad (32)$$

$$\mathbf{F}^{\text{MS}} = -s \overline{B'_r B'_\phi} \hat{\mathbf{e}}_r - s \overline{B'_\theta B'_\phi} \hat{\mathbf{e}}_\theta, \quad (33)$$

$$\mathbf{F}^{\text{MT}} = -\overline{B}_\phi \overline{\mathbf{B}}_M \quad (34)$$

are the fluxes of the meridional circulation (MC), Reynolds stresses (RS), viscous diffusion (VD), Maxwell stresses (MS), and magnetic tension (MT) respectively. Hereafter the subscript  $M$  indicates the meridional component (e.g.,  $\overline{u}_M = \overline{u}_r \hat{\mathbf{e}}_r + \overline{u}_\theta \hat{\mathbf{e}}_\theta$ ). Note that there is no contribution from the magnetic pressure

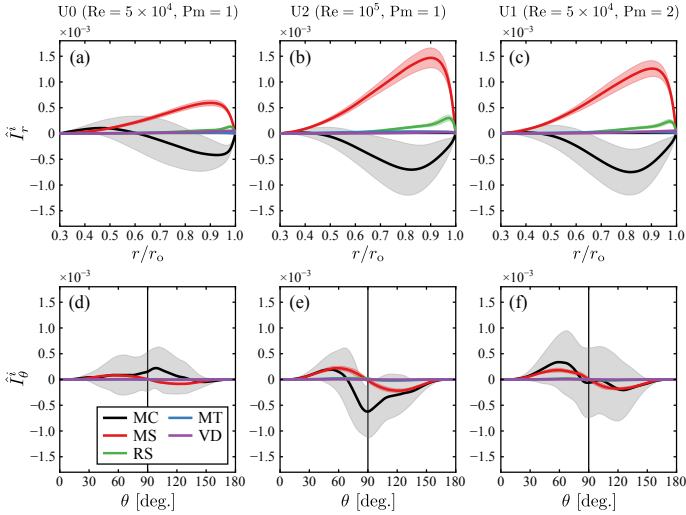


**Fig. 15.** Time averaged integrated fluxes (a–c)  $\hat{I}_r^i$  and (d–f)  $\hat{I}_\theta^i$  for the unstratified runs U0, U2, and U1 (from left to right). The shaded area around each flux contribution shows 1 standard deviation above and below the time average. The scale of the vertical axis is the same in all panels.

$B^2/2$  in Eq. (29) since the longitudinal magnetic pressure gradient vanishes when integrated over  $\phi$ .

We decompose the flux terms Eqs. (30)–(34) into the sum of their radial and latitudinal contributions, that is

$$\mathbf{F}^i = F_r^i \hat{\mathbf{e}}_r + F_\theta^i \hat{\mathbf{e}}_\theta \quad (35)$$

where  $i = \{\text{MC, RS, VD, MS, MT}\}$ ; for example, the Reynolds stresses flux is  $\mathbf{F}^{\text{RS}} = F_r^{\text{RS}} \hat{\mathbf{e}}_r + F_\theta^{\text{RS}} \hat{\mathbf{e}}_\theta$ , where  $F_r^{\text{RS}} = s \overline{u'_r u'_\phi}$  and  $F_\theta^{\text{RS}} = s \overline{u'_\theta u'_\phi}$ . To assess the net AM transport in the radial and latitudinal directions, following Brun & Toomre (2002), we integrate  $F_r^i$  and  $F_\theta^i$  over spherical surfaces of varying radii and over cones of varying inclination respectively,

$$I_r^i(r, t) = \int_0^\pi F_r^i(r, \theta, t) r^2 \sin \theta d\theta \quad (36)$$

and

$$I_\theta^i(\theta, t) = \int_{r_i}^{r_o} F_\theta^i(r, \theta, t) r \sin \theta dr. \quad (37)$$

We then time average these integrated fluxes, obtaining  $\hat{I}_r^i$  and  $\hat{I}_\theta^i$  respectively. In the unstratified dynamo runs, the time averages are calculated over quasi steady states generally covering intervals  $\Delta t$  of a few hundreds of eddy turnover times  $\tau_{\text{eddy}}$  (Table 1). In the stratified runs the turbulence is transient and no steady state is reached, so that the time averaging interval  $\Delta t$  is defined by periods, after the initial transient, where the turbulent magnetic energy does not decay significantly. Such periods cover at least  $56 \tau_{\text{eddy}}$  (Table 1), which still ensures a robust statistics for the turbulence.

### 6.1. Unstratified dynamo runs

First, we analyze the AM transport in the unstratified dynamo runs described in Sects. 5.1–5.3. Figures 15a,d present the time averaged integrated fluxes  $\hat{I}_r^i$  and  $\hat{I}_\theta^i$  in the fiducial dynamo run U0. In both directions, the Maxwell stresses (red lines) and meridional circulation (black lines) fluxes largely dominate over

all the other contributions. In the radial direction, the third largest contribution is the Reynolds stresses flux  $\hat{I}_r^{\text{RS}}$  (green line in Fig. 15a) with a peak amplitude more than 4 times lower than the one of the Maxwell stresses flux  $\hat{I}_r^{\text{MS}}$ . Viscous diffusion and magnetic tension come next, with peak amplitudes of  $\hat{I}_r^{\text{VD}}$  and  $\hat{I}_r^{\text{MT}}$  about 10 and 30 times smaller than the one of  $\hat{I}_r^{\text{MS}}$ . In the latitudinal direction, the Reynolds stresses, viscous diffusion and magnetic tension fluxes all have comparable amplitudes and, similarly to the radial fluxes, their peak values are one order of magnitude lower than  $\hat{I}_\theta^{\text{MS}}$ .

The color shaded areas in Figs. 15a,d show the 1 standard deviation intervals around the time averaged fluxes and evidence that the temporal variability of the meridional circulation fluxes is much higher than the one of all the other terms. This high variability is due to an oscillatory behavior of the meridional flow (dotted red line in Fig. 8) where the dominant large scale meridional circulation cells characterizing the steady state solution (black isocontours in Fig. 9c) are regularly replaced by new ones of opposite sign. These new meridional circulation cells are generated by radial flow plumes arising at mid and high latitudes in the inner fluid regions.

Since the radial fluxes of the prevailing Maxwell stresses and meridional circulation dominate over the respective latitudinal contributions, the transport of AM mainly occurs in the radial direction. The Maxwell stresses transport AM radially outward since  $\hat{I}_r^{\text{MS}} > 0$ . The meridional circulation contributes to the outward transport in the internal fluid regions where  $r/r_o \lesssim 0.6$ , while it opposes in the external regions at larger radii (black line in Fig. 15a). It is not surprising that the meridional flow contributes to the radial transport. In fact, the radial length scales of the meridional circulation cells are comparable to the characteristic scale of the background shear  $l_{\Delta\Omega} \approx r_o$  (Fig. 9c, black isocontours).

The larger amplitudes of  $\hat{I}_r^{\text{MS}}$  with respect to  $\hat{I}_r^{\text{MC}}$  suggest a net outward AM transport. This is confirmed by an additional numerical experiment that we performed by stopping the forcing ( $\mathbf{f} = \mathbf{0}$ ) during the quasi steady evolution of run U0 and letting the azimuthal flow free to evolve. We observe the cylindrical rotation profile flattening over time, with the azimuthal flow decelerating in the interior and accelerating in the equatorial region to reach uniform rotation on a few hundreds of rotation times  $\tau_\Omega$  (Appendix B).

Although negligible relative to the radial one, the transport of AM in the latitudinal direction is also dominated by the Maxwell stresses and the meridional circulation. The former produce an equatorward transport since  $\hat{I}_\theta^{\text{MS}}$  is equatorially antisymmetric, with a positive (negative) contribution in the northern (southern) hemisphere (Fig. 15d, red line).  $\hat{I}_\theta^{\text{MC}}$  is mostly positive (Fig. 15d, black line), hence it contributes to the equatorward transport by the Maxwell stresses in the northern hemisphere and it opposes in the southern one. The amplitudes of  $\hat{I}_\theta^{\text{MC}}$  are generally comparable to the one of  $\hat{I}_\theta^{\text{MS}}$ , except in the equatorial region and at low latitudes in the southern hemisphere where the former is larger.

We now discuss how the transport varies with Re and Pm. The middle and right panels of Fig. 15 display the time averaged integrated fluxes of the dynamo runs U2 and U1 respectively, which we discussed in Sects. 5.2 and 5.3. Relative to the fiducial dynamo run U0, run U2 has a larger Re of  $10^5$  and run U1 a larger Pm of 2. Similarly to the fiducial dynamo, the radial transport in these runs dominates over the latitudinal one and we therefore discuss only the former in the following (Figs. 15b,c,e,f). The net transport occurs radially outward due

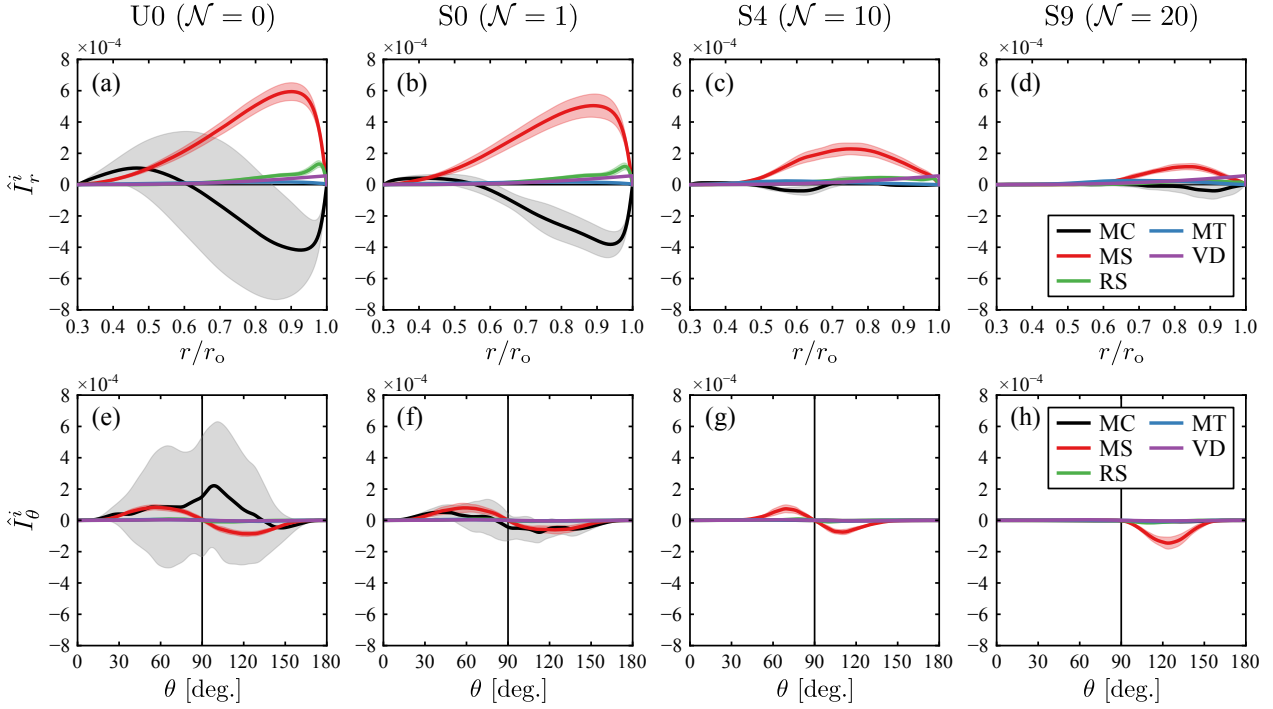


**Fig. 16.** Same as Fig. 15 but for the three stratified runs S0, S4, and S9 at  $\text{Pr} = 10^{-3}$  and  $\mathcal{N} = 1, 10,$  and  $20$  respectively (second to fourth from left panels). The leftmost panels show the unstratified fiducial dynamo run U0 for the sake of comparison. All runs are at  $\text{Re} = 5 \times 10^4$  and  $\text{Pm} = 1$ .

to the prevailing radial Maxwell stresses (Fig. 15b). The peak amplitudes of  $\hat{I}_r^{\text{MS}}$  in runs U2 and U1 are, respectively, about 3 and 2 times higher than the one of run U0, which suggest similar variations in the AM transport efficiency. The time averaged rms turbulent field strengths  $B'_{\text{rms}}$  of runs U2 and U1 are 50% and 41% larger than the one of run U0 respectively, which contributes to explain the observed variations in the Maxwell stresses flux (Table 2). The time averaged rms turbulent flow velocity  $u'_{\text{rms}}$  in these runs is also a few tens of percent higher than the one of run U0 and contribute to explain the increase of the radial Reynolds stresses flux  $\hat{I}_r^{\text{RS}}$  (green lines in Figs. 15b,c).

Similarly to run U0, the meridional circulation in runs U2 and U1 opposes the radial transport by the Maxwell stresses over most of the fluid domain (black lines in Figs. 15b,c). The meridional circulation in these runs is still large scaled and its rms amplitude  $\bar{u}_{\text{M,rms}}$  is about 20% higher than the one of run U0 (Table 2), which can explain the observed variations of  $\hat{I}_\theta^{\text{MC}}$ . These faster meridional flows may result from the higher Reynolds and Maxwell stresses which contribute to the meridional circulation maintenance (see, e.g., Miesch 2005). Likewise to run U0, viscous diffusion and magnetic tension play a negligible role in the transport. Similar variations of the flux contributions with  $\text{Pm}$  are obtained at  $\text{Re} = 10^5$  by comparing run U2 with run U3 at  $\text{Pm} = 0.6$  (not shown).

The weaker dependence of the Reynolds and Maxwell stresses on  $\text{Pm}$  than on  $\text{Re}$  that we just discussed qualitatively agrees with previous results obtained from local and global simulations of unstratified MRI turbulence. Guseva et al. (2017b) showed that the transport coefficient, the sum of the Reynolds and Maxwell stresses, of AMRI turbulence in Taylor–Couette flow scales as  $\text{Pm}^{1/2}\text{Re}$  when  $\text{Rm} \gtrsim 10^2$ . Local shearing box simulations with zero net flux suggest a similar scaling with  $\text{Pm}$ , although the variation with  $\text{Re}$  is much weaker than the linear one obtained for Taylor–Couette flow (Lesur & Longaretti 2007).

## 6.2. Stably stratified runs

By weakening radial motions, stable stratification modifies the transport of AM. Here we discuss how the transport varies with stratification considering the three runs S0, S4, and S9 ( $\text{Pr} = 10^{-3}$  and  $\mathcal{N} = 1, 10,$  and  $20$  respectively) discussed in Sect. 5.4. Figure 16 displays the time averaged integrated fluxes  $\hat{I}_r^i$  and  $\hat{I}_\theta^i$  in these runs, together with the fiducial dynamo run U0 in the two leftmost panels for the sake of reference. In the weakly stratified run S0, the transport occurs similarly to the unstratified case. Only a small decrease of the dominant Maxwell stresses and meridional circulation fluxes is observed (red and black lines in Figs. 16b,f). However, the meridional circulation shows a much weaker variability, as demonstrated by the small 1 standard deviation intervals around  $\hat{I}_r^{\text{MC}}$  and  $\hat{I}_\theta^{\text{MC}}$  (gray shaded regions in Figs. 16b,f), since the oscillatory behavior observed for run U0 is absent.

Increasing  $\mathcal{N}$  to 10 (run S4) produces a sizeable decrease of the radial Maxwell stresses flux  $\hat{I}_r^{\text{MS}}$  (red line in Fig. 16c). The latitudinal Maxwell stresses flux  $\hat{I}_\theta^{\text{MS}}$  is confined at low to intermediate latitudes (red line in Fig. 16g), which correlates with the locations where the instability is active (Fig. 13e). The transport by the meridional flow becomes almost negligible (black lines in Figs. 16c,g) since radial flow motions are severely limited by the stabilizing buoyancy force. The meridional flow amplitude  $\bar{u}_{\text{M,rms}}$  is indeed 2.5 times smaller than the one of the weakly stratified run S0 (Table 2) and multiple meridional circulation cells elongated in the latitudinal direction are observed (black isocontours in Fig. 13k). The horizontal flow length scale  $l_{u,\perp}/d$  increases to 0.22, while is smaller at 0.17 in run S0 as expected.

In run S9 at  $\mathcal{N} = 20$ ,  $\hat{I}_r^{\text{MS}}$  further weakens and its peak amplitude becomes comparable to the respective latitudinal contribution  $\hat{I}_\theta^{\text{MS}}$  (red lines in Figs. 16d,h). The latitudinal Maxwell stresses flux is concentrated in the southern hemisphere at the locations where the axisymmetric azimuthal field is strong enough to support AMRI (Sect. 5.4). The transport by the



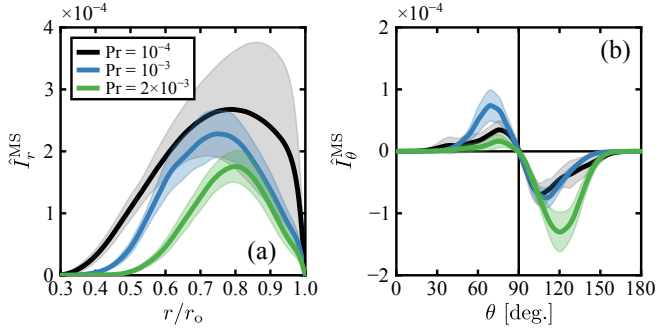


**Fig. 17.** Time averaged integrated (a) radial and (b) latitudinal Maxwell stresses fluxes in runs S3, S4, and S5, which are at  $\text{Pr} = 10^{-4}$ ,  $10^{-3}$ , and  $2 \times 10^{-3}$  respectively. The other parameters are  $\text{Re} = 5 \times 10^4$ ,  $\text{Pm} = 1$ , and  $\mathcal{N} = 10$ . The shaded areas show 1 standard deviation above and below the time averages.

meridional circulation remains very weak as in run S4 (black lines in Figs. 16d,h) and no significant variation in the meridional flow amplitude is observed (Table 2). However, the meridional circulation cells become thinner in the radial direction as expected (black isocontours in Fig. 13l).

Similar results on the variation of the integrated fluxes are obtained when strengthening buoyancy effects by reducing thermal diffusion, that is when increasing  $\text{Pr}$  at fixed  $\mathcal{N}$ . Since the Maxwell stresses dominate the transport, we discuss only their variation with  $\text{Pr}$  here. Figure 17 presents  $\hat{F}_r^{MS}$  and  $\hat{F}_\theta^{MS}$  in runs S3, S4, and S5 at  $\mathcal{N} = 10$  and  $\text{Pr} = 10^{-4}$ ,  $10^{-3}$ , and  $2 \times 10^{-3}$  respectively. Similarly to the runs discussed above, the radial Maxwell stresses flux prevails over the latitudinal one. The amplitude of  $\hat{F}_r^{MS}$  lowers when  $\text{Pr}$  increases and its distribution shifts toward the outer fluid regions where the instability is active (Fig. 17a). Similarly to what has been observed above for run S9,  $\hat{F}_\theta^{MS}$  concentrates in the southern hemisphere when buoyancy effects are stronger at the larger  $\text{Pr}$  of  $2 \times 10^{-3}$  (green line in Fig. 17b).

In all stratified runs explored here, Reynolds stresses, viscous diffusion and magnetic tension contribute very weakly to the AM transport in both the radial and latitudinal directions. Magnetic tension is the weakest of all contributions since  $\overline{B}_p$  is always small as we discussed in Sect. 5.4.

### 6.3. Turbulent viscosity

We demonstrated above that the AM transport induced by AMRI occurs radially outward and is dominated by the Maxwell stresses when  $\mathcal{N} > 1$ . The meridional circulation contribution is significant only in the unstratified and weakly stratified runs at  $\mathcal{N} = 1$ . To quantify the transport efficiency, we therefore consider the contribution by the radial Maxwell stresses only and we assume the classical turbulent viscosity hypothesis in which AM is transported in the direction of slow rotation,

$$-\frac{1}{\mu_0 \rho} \overline{B'_r B'_\phi} = -\nu_T s \frac{\partial \overline{\Omega}}{\partial r}. \quad (38)$$

Here  $\nu_T$  is the radial turbulent viscosity and  $\overline{\Omega} = \Omega_f$ . We obtain the turbulent viscosity estimate  $\hat{\nu}_T$  from the relation above by taking first a volume average of both members,

$$\nu_T = (\mu_0 \rho)^{-1} \langle \overline{B'_r B'_\phi} \rangle / \langle s \partial \Omega_f / \partial r \rangle, \quad (39)$$

and then by time averaging Eq. (39) over the intervals  $\Delta t$  defined before and listed in Table 1. In runs showing transient turbulence,  $\hat{\nu}_T$  has to be interpreted as an upper estimate for the

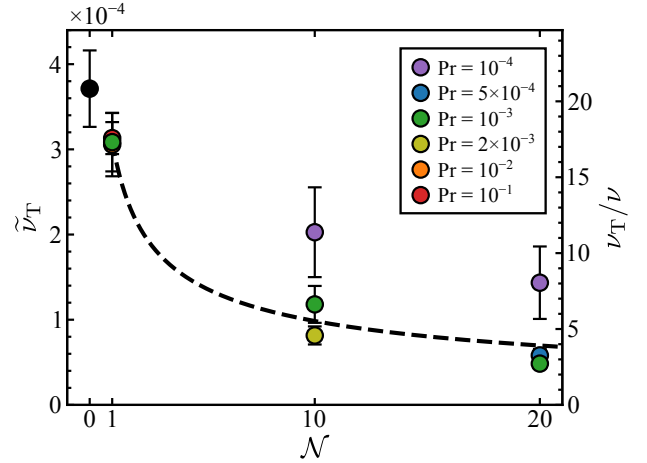


**Fig. 18.** Turbulent viscosity  $\hat{\nu}_T$  as a function of  $\mathcal{N}$  for  $\text{Re} = 5 \times 10^4$  and  $\text{Pm} = 1$ . The symbol color shows the Prandtl number  $\text{Pr}$  as indicated in the legend. The black circle at  $\mathcal{N} = 0$  is the fiducial dynamo run U0. The error bars show 1 standard deviation intervals around the time averages, which are evaluated over the periods  $\Delta t$  listed in Table 1. The dashed curve shows a power law fit  $\hat{\nu}_T = a \mathcal{N}^{-\delta}$  of the stratified runs at  $\text{Pr} = 10^{-3}$ . The best fitting parameters are  $a = 3.1 \times 10^{-4}$  and  $\delta = 0.50$ . The right vertical axis displays the turbulent viscosity in units of the molecular viscosity  $\nu$ .

transport efficiency since the instability decays on timescales longer than  $\Delta t$ . The dimensionless turbulent viscosity estimate is  $\hat{\nu}_T = \hat{\nu}_T / \Delta \Omega r_0^2$ , where we employed the shear timescale  $\tau_{\Delta \Omega} = \Delta \Omega^{-1}$  and the shear length scale  $l_{\Delta \Omega} \approx r_0$  as reference scales.

Figure 18 displays  $\hat{\nu}_T$  as a function of  $\mathcal{N}$  for all unstable runs at  $\text{Re} = 5 \times 10^4$  and  $\text{Pm} = 1$  explored here. The turbulent viscosity lowers when buoyancy effects strengthen, that is when  $\mathcal{N}$  and/or  $\text{Pr}$  increase. The largest value of  $\hat{\nu}_T$  is  $3.7 \times 10^{-4}$  and is obtained for the unstratified fiducial dynamo run U0 as expected (black circle). In the stratified runs at  $\mathcal{N} > 1$ , the turbulent viscosity approaches the unstratified value when  $\text{Pr}$  decreases since thermal diffusion limits the stabilizing buoyancy force. In the weakly stratified runs at  $\mathcal{N} = 1$  the effect of stable stratification on the radial Maxwell stresses is only marginal (Sect. 6.2) and therefore  $\hat{\nu}_T$  shows only a weak decrease relative to the unstratified run.

At fixed Prandtl number  $\text{Pr}$ , the turbulent viscosity  $\hat{\nu}_T$  lowers when increasing  $\mathcal{N}$ . At  $\text{Pr} = 10^{-3}$ , for example,  $\hat{\nu}_T$  varies by roughly a factor 6 in the range of stratification explored. When  $\mathcal{N}$  increases from 1 (run S0) to 10 (run S4), such variation is mostly due to changes in the turbulent field amplitudes. In fact,  $\hat{\nu}_T$  decreases by more than a factor 2 from run S0 to run S4 and  $(B'_{\text{rms}})^2$  lowers by a factor 1.6 (Table 2). The residual turbulent viscosity variation may be an effect of volume averaging. The unstable fluid regions of run S4 are indeed more localized than those of run S0, as already discussed in Sect. 5.4. This is also clearly evidenced by the distribution of  $\hat{F}_r^{MS}$ , the time averaged radial Maxwell stresses flux, which is shown in Figs. 19b,c for these two runs. The smaller turbulent viscosity value of run S9 at  $\mathcal{N} = 20$  instead originates from the weaker spatial correlations of the turbulence, together with a volume averaging effect. In fact, runs S9 and S4 share a similar value of  $B'_{\text{rms}}$  of 0.018 (Table 2) but the peak amplitudes of  $\hat{F}_r^{MS}$  are 40% lower in the former run (Figs. 19c,d).

The variations of  $\hat{\nu}_T$  with  $\text{Pr}$ , observed when  $\mathcal{N} > 1$  is fixed, likewise originate from changes in both the size of the unstable

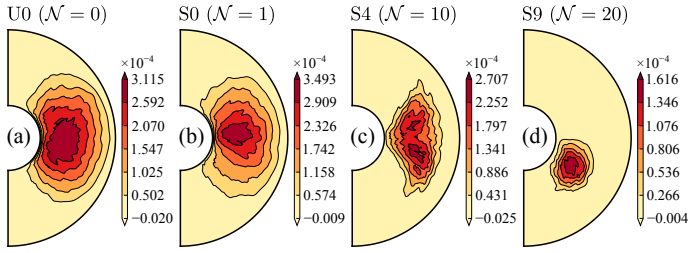


**Fig. 19.** Time averaged radial Maxwell stresses fluxes  $\hat{F}_r^{\text{MS}}$  for (a) the unstratified fiducial dynamo run U0 and (b–d) the stratified runs S0, S4, and S9 at  $\text{Pr} = 10^{-3}$  and  $\mathcal{N} = 1, 10,$  and  $20$  respectively. In all runs,  $\text{Re} = 5 \times 10^4$  and  $\text{Pm} = 1$ .

regions and the spatial correlations of the turbulent field. In these runs, while  $B'_{\text{rms}}$  weakly changes with  $\text{Pr}$  (Table 2), the integrated Maxwell stresses flux  $\hat{F}_r^{\text{MS}}$  reduces when  $\text{Pr}$  increases (Sect. 6.2), which suggests a decrease of the spatial correlations of the turbulent field. The distribution of  $\hat{F}_r^{\text{MS}}$  also narrows as  $\text{Pr}$  increases, which yields smaller values for the volume averaged Maxwell stresses in our turbulent viscosity estimate.

A power law of the form  $\tilde{\nu}_T = a \mathcal{N}^{-\delta}$ , where  $\delta > 0$ , well describes the dependence of the turbulent viscosity on stratification. A least squares fit of the runs at  $\text{Pr} = 10^{-3}$  provides an exponent  $\delta = 0.50$  and a prefactor  $a = 3.1 \times 10^{-4}$  (dashed line in Fig. 18). For AMRI turbulence in Taylor–Couette flow, Spada et al. (2016) suggest a stronger scaling of  $\mathcal{N}^{-1}$ . For a free shear, Jouve et al. (2020) demonstrated that some of the linear properties of AMRI, such as the instability threshold and the range of linearly unstable modes, depend only on the parameter combination  $\mathcal{N}^2 \text{Pr}$ . However, our simulations indicate that this is not the case for the nonlinear evolution of AMRI and for the AM transport efficiency.

## 7. Transport of chemical elements

### 7.1. Model formulation

We assume the light stellar chemical elements to contaminate the turbulent fluid flow as a passive scalar, that is their concentration is so low that they have no dynamical influence on the fluid motion itself. The equation of evolution of the chemical concentration  $c$  is

$$\frac{\partial c}{\partial t} + (\mathbf{u} \cdot \nabla) c = \frac{1}{\text{Sc Re}} \nabla^2 c, \quad (40)$$

which is solved together with Eqs. (2)–(4). Here the Schmidt number

$$\text{Sc} = \frac{\nu}{D_c} \quad (41)$$

is the ratio of the fluid kinematic viscosity  $\nu$  to the molecular chemical diffusivity  $D_c$ . We consider  $\text{Sc} = 1$  so that the diffusion timescale of the chemicals  $d^2/D_c$  and the viscous timescale of the flow  $\tau_\nu = d^2/\nu$  are equal. We assume no sources nor sinks of the chemical elements from the boundaries by imposing a zero chemical concentration flux  $\partial c/\partial r = 0$  at  $r = r_i$  and  $r_o$ . The initial distribution of the chemical concentration is the spherically symmetric Gaussian

$$c(r, t = t_0) = \frac{1}{C_0} \exp\left[-\frac{(r - r_0)^2}{2\sigma_0^2}\right]. \quad (42)$$

The distribution is centered at mid depth in the fluid domain,  $r_0 = (1/\chi - 1)^{-1} + 1/2$ , and has a full width at half maximum of

**Table 3.** Input parameters and output diagnostics of the simulations where a passive scalar is introduced.

Name	$\mathcal{N}$	$\text{Pr}$	Run	$t_0$	$\tau_M/\tau_\Omega$	$\tilde{D}_T \times 10^5$
C0	0	–	U0	1764.1	117.5	$18.9 \pm 6.8$
C1	1	$10^{-3}$	S0	2151.3	139.8	$16.6 \pm 0.7$
C2	1	$10^{-2}$	S1	1811.2	187.2	$12.0 \pm 1.4$
C3	1	$10^{-1}$	S2	2092.9	277.4	$8.3 \pm 0.8$
C4	10	$10^{-4}$	S3	1400.2	353.9	$10.6 \pm 1.5$
C5	10	$10^{-3}$	S4	2625.1	246.3	$5.4 \pm 0.6$
C6	10	$2 \times 10^{-3}$	S5	2466.5	435.3	$3.9 \pm 0.4$
C7	20	$10^{-4}$	S7	1755.6	249.9	$7.8 \pm 1.1$
C8	20	$5 \times 10^{-4}$	S8	1902.6	543.1	$3.3 \pm 0.2$
C9	20	$10^{-3}$	S9	2282.4	648.3	$2.7 \pm 0.2$

**Notes.**  $t_0$  is the time of the simulation runs indicated in the fourth column at which the passive scalar is introduced.  $\tau_M$  is the meridional flow timescale calculated as explained in the main text.  $\tilde{D}_T$  is the estimated turbulent chemical diffusivity and the error denotes 1 standard deviation in time. All runs are at  $\text{Re} = 5 \times 10^4$  and  $\text{Pm} = 1$ .

$\delta_0/d = 1/10$ , which corresponds to a variance  $\sigma_0^2 = (\sigma_0^*/d)^2 \approx 1.8 \times 10^{-3}$ . The total mass of the chemicals in the fluid domain  $C_0 = \int c(t = t_0) dV$  is a conserved quantity and serves as a normalization constant here.

The chemical layer Eq. (42) is introduced during the turbulent AMRI evolution of the unstratified fiducial dynamo run U0 and of all the stratified runs at the times  $t = t_0$  listed in Table 3. In the following sections we study the turbulent transport of the chemicals, we estimate its efficiency and we compare the results with the AM transport.

### 7.2. Estimate of the turbulent chemical diffusivity

First, we examine the temporal evolution of the azimuthally averaged (mean) chemical concentration  $\bar{c}$  in our numerical simulations and analyze the turbulent transport. If the turbulent transport occurs as a diffusive process, the radial distribution of  $\bar{c}$  remains Gaussian over time and its variance  $\sigma^2$  increases linearly. The rate at which  $\sigma^2$  grows defines the radial turbulent chemical diffusivity

$$D_T = \frac{1}{2} \frac{d\sigma^2}{dt}. \quad (43)$$

In all runs explored here, the turbulent transport of the mean chemical concentration is diffusive during the initial stages of its evolution. Figure 20a displays the evolution of the radial profile of the horizontally averaged mean chemical concentration  $\langle \bar{c} \rangle$  in run C5 ( $\mathcal{N} = 10$  and  $\text{Pr} = 10^{-3}$ ) as an example. The distribution remains Gaussian for a period of about  $150 \Omega_a^{-1}$  after  $t_0$  and its variance  $\sigma^2$  increases linearly as expected (Fig. 20c; see also the snapshots of  $\bar{c}$  in Figs. 21a–c). We calculated the turbulent chemical diffusivity  $D_T$  from Eq. (43) by performing a time average of  $d\sigma^2/dt$  over this interval (dashed line in Fig. 20c), which covers 12 eddy turnover times  $\tau_{\text{eddy}}$  (see the upper horizontal axis of Fig. 20c). This procedure yields a dimensionless chemical diffusivity  $\tilde{D}_T = D_T/\Delta\Omega r_o^2$  of  $5.4 \times 10^{-5}$ . The last column of Table 3 reports the estimates  $\tilde{D}_T$  for all runs explored here.

In run C5, deviations from a diffusive transport begin at time  $t - t_0 \approx 200$  when  $\sigma^2$  starts to level off and does not evolve linearly anymore (Fig. 20c). At  $t - t_0 = 400$  the distribution of the mean concentration becomes decisively non-Gaussian and

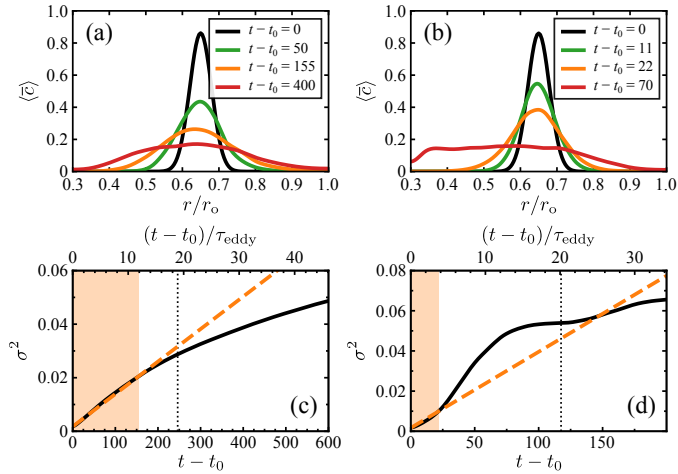


**Fig. 20.** Chemical turbulent transport for run C5 at  $\mathcal{N} = 10$  and  $\text{Pr} = 10^{-3}$  (left panels) and for the unstratified run C0 (right panels). (a,b) Radial distribution of the horizontally averaged mean chemical concentration  $\langle \bar{c} \rangle$  at the times  $t - t_0$  indicated in the legend. The first three times cover the diffusive phase of the transport. (c,d) Variance  $\sigma^2$  of the mean chemical concentration  $\bar{c}$  as a function of  $t - t_0$ . The dashed line is defined by the time average of  $d\sigma^2/dt$  evaluated over the diffusive phase of the transport (orange shaded background). The vertical dotted line marks the time  $t - t_0 = \tau_M/\tau_\Omega$  after which the meridional flow is expected to dominate the transport. Here  $\tau_M$  is the meridional flow timescale estimated as explained in the main text. The upper horizontal axis displays time scaled in units of the eddy turnover time  $\tau_{\text{eddy}}$ .

its flanks reach the boundaries (Fig. 20a, red line). A snapshot of  $\bar{c}$  at this time evidences that the meridional circulation contributes, on such longer timescales, to expel the chemicals from the central parts of the fluid domain, accumulating them at high latitudes in the southern hemisphere (Fig. 21d). We estimated a characteristic timescale for the meridional flow in the region of the chemical layer as  $\tau_M = \int_{r_0-\sigma_0}^{r_0+\sigma_0} dr / \langle \bar{u}_M \rangle$ , where  $\langle \bar{u}_M \rangle$  is the horizontally averaged meridional velocity at  $t = t_0$ . In run C5  $\tau_M = 246 \Omega_a^{-1}$  (vertical dotted line in Fig. 20c), which agrees well with the timescale on which  $\sigma^2$  starts to deviate from the initial diffusive evolution.

When buoyancy effects weaken by considering lower  $\mathcal{N}$  and/or  $\text{Pr}$ , the meridional flow timescale  $\tau_M$  decreases as expected (Table 3) and therefore the transport of the chemicals by the meridional flow takes over the turbulent one earlier during the evolution. Nonetheless, the shortest period of diffusive evolution in our stratified simulations, obtained for run C1 ( $\mathcal{N} = 1$  and  $\text{Pr} = 10^{-3}$ ), covers about  $8 \tau_{\text{eddy}}$ , which still ensures a robust statistics for the turbulence.

In the unstratified run C0 the diffusive phase covers an even shorter interval of  $3.7 \tau_{\text{eddy}}$  (orange shaded area in Fig. 20d). The meridional flow timescale  $\tau_M$  reduces to  $118 \Omega_a^{-1}$  and  $\langle \bar{c} \rangle$  becomes decisively non-Gaussian already at  $t - t_0 = 70$  (Fig. 20b, red line; Fig. 21h). The estimate of  $\tilde{D}_T$  in run C0 is therefore less accurate than all the other runs where a reliable measurement is instead achieved. In this run the standard deviation of  $\tilde{D}_T$  is as large as 31% of the turbulent diffusivity value itself. In the runs at  $\mathcal{N} = 10$  and 20 and higher  $\text{Pr}$ , the standard deviation is instead of only a few percent of  $\tilde{D}_T$  since the diffusive phase lasts more than  $10 \tau_{\text{eddy}}$  (Table 3). For a diffusive transport, a certain degree of scale separation between the initial chemical layer width  $\delta_0$  and the characteristic radial length scale of the turbulence is required. While in runs at  $\mathcal{N} > 1$  such a scale separation

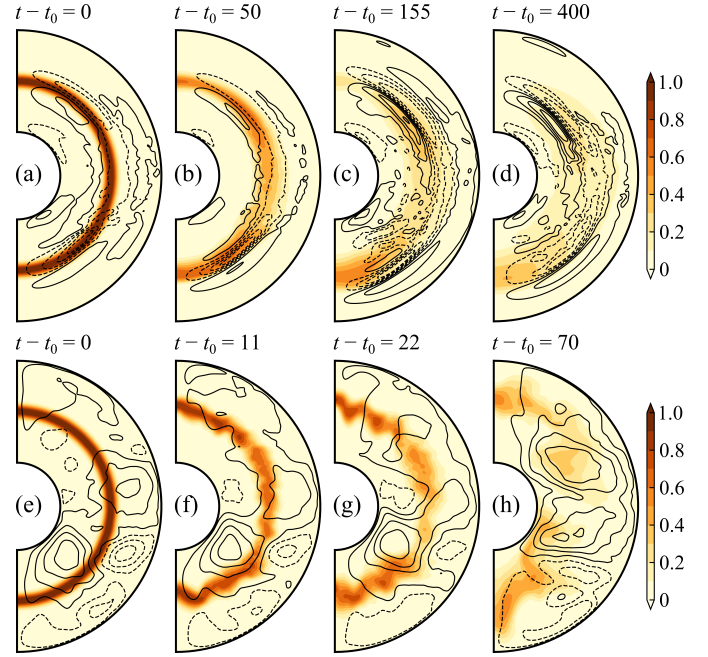


**Fig. 21.** Snapshots of the mean chemical concentration  $\bar{c}$  in runs C5 (top panels) and C0 (bottom panels) at the times  $t - t_0$  of Figs. 20a,b. The mean concentration  $\bar{c}$  is normalized with its maximum value at  $t = t_0$  here.

is verified, in run C0 this becomes only marginally satisfied, as evidenced by the strong latitudinal variations of  $\bar{c}$  (Figs. 21f,g), and may cause additional accuracy loss in our estimate of the turbulent diffusivity.

### 7.3. Chemical and angular momentum transport

We now discuss how the efficiency of the chemical turbulent transport varies with the effect of stratification. Figure 22a shows that  $\tilde{D}_T$  lowers when buoyancy effects strengthen either by increasing  $\mathcal{N}$  and/or  $\text{Pr}$ . The two most weakly stratified runs at  $\mathcal{N} = 1$  with  $\text{Pr} = 10^{-3}$  and  $10^{-2}$  have values of  $\tilde{D}_T$  comparable to the unstratified case (black circle) within their 1 standard deviation intervals. In the runs at  $\mathcal{N} = 10$  and 20, as discussed in the previous section, the turbulent diffusivity estimates become more accurate due to the longer diffusion phase and the uncertainties are generally smaller than the symbol sizes themselves. As with the turbulent viscosity, a power law well describes the dependence of the chemical diffusivity on stratification. A power law fit of the stratified runs at  $\text{Pr} = 10^{-3}$  provides  $\tilde{D}_T = 1.7 \times 10^{-4} \mathcal{N}^{-0.54}$  (dashed line in Fig. 22a). The exponent of  $\mathcal{N}$  is very similar to the one obtained for the turbulent viscosity (Sect. 6.3).

The turbulent Schmidt number

$$\text{Sc}_T = \frac{\tilde{\nu}_T}{\tilde{D}_T} \quad (44)$$

measures the efficiency of the AM transport relative to the one of the chemical elements. Figure 22b displays  $\text{Sc}_T$  as a function of  $\mathcal{N}$  for all simulation runs and shows that this is always larger than 1 and does not vary much with increasing buoyancy effects in the ranges of  $\mathcal{N}$  and  $\text{Pr}$  explored. The value  $\text{Sc}_T = 1.96 \pm 0.75$  of the unstratified run C0 (black circle) encompasses all the other estimates obtained for the stratified runs, except for the case at  $\mathcal{N} = 1$  and  $\text{Pr} = 10^{-1}$  which is larger at  $\text{Sc}_T = 3.8$ . Our

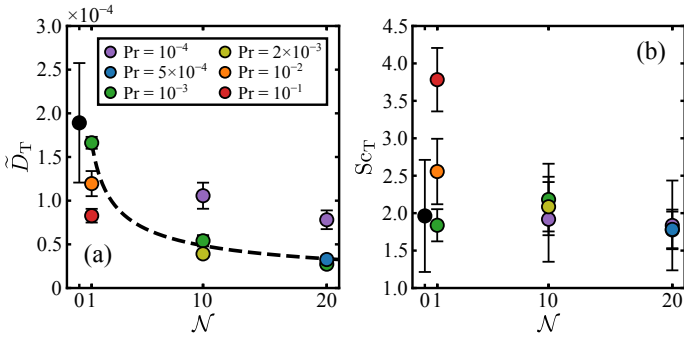


**Fig. 22.** Efficiency of the turbulent transport of the chemicals and comparison with the one of angular momentum. (a) Turbulent chemical diffusivity  $\bar{D}_T$  and (b) turbulent Schmidt number  $Sc_T$  as a function of  $N$ . The black circle shows the unstratified fiducial dynamo run U0. The symbol color of the stratified runs codes the Prandtl number  $Pr$  as indicated in the legend in (a). Error bars in (a) show 1 standard deviation intervals around the time averaged turbulent diffusivity values. The dashed line in (a) displays a power law fit of the stratified runs at  $Pr = 10^{-3}$ , that is  $\bar{D}_T = 1.7 \times 10^{-4} N^{-0.54}$ . The errors in (b) are obtained by propagating the uncertainties of the turbulent viscosity  $\tilde{\nu}_T$  and of the turbulent diffusivity  $\bar{D}_T$ .

simulations therefore suggest that AMRI turbulence induces a transport of AM which is systematically stronger than the one of chemical elements. This is expected since the Maxwell stresses, which dominate the transport of AM in our runs and do not directly influence the one of chemical elements, are generally stronger than the Reynolds stresses (Sects. 6.1 and 6.2), which instead regulate the chemical transport. However, we note that  $R = (\mu_0 \rho)^{-1} \langle B'_r B'_\phi \rangle / \langle u'_r u'_\phi \rangle$ , the ratio of the volume averaged radial Maxwell stresses to the volume averaged radial Reynolds stresses, is always larger than 5 (Table 2) and overestimates the relative transport efficiency measured by  $Sc_T$ .

## 8. Summary and discussion

Additional transport processes beyond atomic diffusion and standard hydrodynamical mechanisms, such as meridional circulation and shear turbulence, are required to explain the observed rotational and chemical evolution of low-mass stars. MHD turbulence is regarded as one of the primary processes to enhance the transport in radiative stellar interiors. In this work we investigated numerically the transport of AM and chemical elements due to azimuthal MRI in a spherical shell where cylindrical differential rotation is forced.

We first considered an unstratified flow at a magnetic Prandtl number  $Pm$  of 1 and explored the stability of purely axisymmetric toroidal field configurations to weak nonaxisymmetric perturbations. The parameter regime where we observe AMRI agrees well with predictions obtained from a local linear stability analysis and with the global linear analysis results of Guseva et al. (2017b) who analyze Taylor–Couette flow with an imposed field. Our AMRI runs are characterized by values of  $Le_\phi^{\max}$  not smaller than about  $5 \times 10^{-3}$ , otherwise diffusive effects stabilize the system, and not larger than about 0.5, or else the nature of the instability changes and TI is found. Here  $Le_\phi^{\max}$  is the maximum value in the fluid domain of the ratio of the Alfvén frequency of the axisymmetric azimuthal field  $\omega_{A\phi} = \bar{B}_\phi / (\mu_0 \rho)^{1/2} d$  to the reference rotation rate  $\Omega_a$ .

Next, we explored the nonlinear evolution of the instability in these unstratified runs. At  $Pm = 1$ , we observe self-sustained

dynamo action when  $Re \geq 5 \times 10^4$  and the azimuthal field strength of the perturbed axisymmetric solution is large enough (runs U0 and U2). At the larger  $Re$  of  $10^5$ , we find dynamo action down to  $Pm = 0.6$  (run U3). These simulations are the first global MRI dynamos ever reported at such low values of  $Pm$ . We obtain transient turbulence in all the other unstable runs.

We then examined the effect of thermal stable stratification on unstratified AMRI turbulence at  $Re = 5 \times 10^4$  and  $Pm = 1$ . To this end, we varied  $N = N/\Omega_a$ , the ratio of the Brunt–Väisälä frequency to the reference rotation rate, from 1 to 20 and the Prandtl number  $Pr$  in the range  $10^{-4} - 10^{-1}$ . When increasing buoyancy effects, the turbulence becomes less isotropic and homogeneous. However, when  $Pr$  is too large, thermal diffusion cannot limit the stabilizing buoyancy force anymore and AMRI is suppressed. In our most stratified unstable runs, we observe instability structures elongated in the latitudinal direction and unstable regions localized in the southern hemisphere where the axisymmetric azimuthal field is strong enough to support AMRI. All the stratified runs show transient turbulence, although in a few cases the numerical integration time is too short to test for dynamo action. We argue that, by limiting radial flow motions, stable stratification reduces the effective magnetic Reynolds number  $Rm_{\text{eff}}$  below the critical value for dynamo onset, which is of about 800 based on the unstratified runs. Nonetheless, the magnetic and kinetic energies show an oscillatory behavior typical of  $\alpha\Omega$ -dynamos that has been reported before (e.g., Reboul-Salze et al. 2022).

We explored the transport of AM in the unstratified dynamo solutions and in the stratified runs, showing that it occurs radially outward and is largely dominated by the Maxwell stresses when  $N \geq 10$ . The meridional circulation opposes to the radial transport by the Maxwell stresses only when no stratification is present or is weak at  $N = 1$ . We quantified the radial AM transport by estimating the turbulent viscosity  $\tilde{\nu}_T = \nu_T / \Delta\Omega r_o^2$ , where  $\Delta\Omega$  is the global rotation contrast and  $r_o$  the outer boundary radius, and we show that it decreases when buoyancy effects strengthen. Within the explored range of parameters, the turbulent viscosity variations are well described by the power law  $\tilde{\nu}_T = a N^{-1/2}$ , where  $a = 3.1 \times 10^{-4}$ .

Finally, we investigated the turbulent transport of a passive scalar. After demonstrating that this occurs as a diffusive process, we estimated the diffusion coefficient  $\bar{D}_T$ . In the range of parameters explored,  $\bar{D}_T$  varies with buoyancy effects similarly to the turbulent viscosity  $\tilde{\nu}_T$  but its magnitude is systematically lower. A power law  $\bar{D}_T = 1.7 \times 10^{-4} N^{-0.54}$  well describes our simulation data so that the turbulent Schmidt number  $Sc_T = \tilde{\nu}_T / \bar{D}_T$  is always of about 2 in the range of parameters explored. When buoyancy effects are high enough and the AM transport is dominated by the turbulent magnetic field fluctuations and the one of the chemicals by the flow fluctuations, we tested whether the ratio of the radial Maxwell stresses to the radial Reynolds stresses is a good proxy for  $Sc_T$ . We find that this ratio generally overestimates  $Sc_T$  by roughly a factor 3 in our simulations.

As far as an application to stars is concerned, there are several limitations to the setup explored here. First, we examined MRI of purely toroidal fields whereas magnetic field configurations with both toroidal and poloidal components are expected in stellar interiors. Secondly, the background differential rotation profile and its amplitude may not be representative of the shear in stellar interiors. We also ignored the additional stabilizing effect of chemical buoyancy in the momentum equation. Relaxing one or more of these assumptions may yield to turbulent diffusion coefficients that differ from those estimated here.

However, other fluid properties employed in our simulations approach those expected in certain regions of stellar interiors.

For example, the values of the molecular diffusivity ratios and of the stable stratification are close to those of the electron-degenerate cores of red giants and of the nondegenerate radiative outer regions of these stars, respectively. In fact, the Prandtl number  $Pr$  is typically  $\sim 10^{-3}$  in degenerate red giant cores (Garaud et al. 2015) and the magnetic Prandtl number  $Pm$  ranges between  $10^{-1}$  and  $10$  (Rüdiger et al. 2015). The nondegenerate radiative regions immediately above the hydrogen burning shell are less dense than the degenerate zones below and expand during their evolution, hence the thermal component of the Brunt–Väisälä frequency  $N_T$  is relatively low at  $\sim 10^{-3} \text{ s}^{-1}$  in the subgiant phase and further decreases to about  $5 \times 10^{-4} \text{ s}^{-1}$  on the red giant branch (Talon & Charbonnel 2008). The typical angular rotation frequency  $\Omega/2\pi$  of the cores of these stars is roughly in the range 600–700 nHz (Deheuvels et al. 2014; Gehan et al. 2018), which yields  $N_T/\Omega \approx 100\text{--}200$ , that is only from 5 to 10 times larger than the highest value of  $N = 20$  employed in our simulations. Such moderate values of  $N_T/\Omega$  also characterize the interior of pre-MS stars (Gouhier et al. 2021).

However, in both the radiative regions of red giants above and below the hydrogen burning shell, the values of the molecular diffusivity ratios and  $N_T/\Omega$  cannot be captured simultaneously. In the degenerate cores,  $N_T/\Omega$  is as large as  $\sim 10^3$  during the subgiant phase and increases to  $10^4$  in evolved red giants (Talon & Charbonnel 2008). In the outer nondegenerate layers, where the diffusivities are dominated by radiative and collisional contributions only,  $Pr$  and  $Pm$  drop to about  $10^{-7}$  and  $10^{-2}$  respectively (Garaud et al. 2015; Rüdiger et al. 2015).

We show that the turbulent viscosity in our simulations scales with  $N^{-1/2}$ , which is slower than the  $N^{-1}$  scaling suggested for AMRI in Taylor–Couette flow with imposed current-free magnetic fields (Spada et al. 2016). Assuming that our scaling prediction  $\tilde{\nu}_T = 3.1 \times 10^{-4} N^{-1/2}$  is confirmed for larger values of the stable stratification than those explored here, we obtain a turbulent viscosity  $\nu_T = \tilde{\nu}_T r_o^2 \Delta\Omega$  in the range  $2\text{--}7 \times 10^8 \text{ cm}^2 \text{ s}^{-1}$  for the degenerate cores of subgiants and red giants. For  $N$ , here we used the values of  $N_T/\Omega$  discussed above; for the shear contrast  $\Delta\Omega/2\pi$  we considered the typical angular velocity difference between the core and the envelope of subgiants of 900 nHz, and for the radius of the radiative region  $r_o = 0.05 R_\odot$ , which is 2% of the typical radius of subgiants  $R = 2.5 R_\odot$  (Deheuvels et al. 2014). Such a high turbulent viscosity value enforces solid body rotation in the degenerate core on a timescale of around 2000 yr, which is not incompatible with the observations. It is indeed likely that the observed radial shear of subgiants is localized around the hydrogen burning shell, hence above the degenerate core which may be in rigid rotation instead (Deheuvels et al. 2014). This observational evidence is further supported by the fact that stable stratification peaks at the hydrogen burning shell, where the transport of AM would be the slowest (Fuller et al. 2019). In regions around the hydrogen burning shell, chemical stratification largely dominates over the thermal contribution. The thermal Brunt–Väisälä frequency  $N_T$  is lower in these regions than in the core so that our scaling predicts even larger turbulent viscosity values, hence faster transport than the one estimated above. Stellar evolution models that reproduce the rotational evolution of low-mass evolved stars suggest a significantly smaller turbulent diffusion coefficient which increases monotonically from  $10^2 \text{ cm}^2 \text{ s}^{-1}$  in early subgiants to almost  $10^6 \text{ cm}^2 \text{ s}^{-1}$  at the end of the red giant phase (Spada et al. 2016; Moyano et al. 2022).

Our simulations show that the transport of AM due to AMRI may be more efficient than the one induced by TI. The theory of

Fuller et al. (2019) for TI-driven dynamo action predicts that the turbulent viscosity scales as  $(N_T/\Omega)^{-2}$ , whereas here we obtain a power exponent of  $-1/2$  for AMRI. TI dynamo action may have been recently identified in global numerical simulations (Petitdemange et al. 2023), but robustly testing the proposed turbulent viscosity scalings requires further study.

The magnetic field strengths recently measured in red giant cores can be directly compared to our numerical simulation results in terms of the radial Lenz number  $Le_r^{\text{rms}}$ , the ratio of the local Alfvén frequency based on the rms radial field  $B_r^{\text{rms}}/(\mu_0\rho)r$  to the rotation rate  $\Omega$ . In the 13 red giants where magnetic field measurements exist so far,  $Le_r^{\text{rms}}$  ranges between 0.05 and 0.25 at the hydrogen burning shell, the region of maximum sensitivity for the asteroseismic inversions (Li et al. 2023). Such strong field amplitudes are incompatible with those expected from TI dynamo action which predicts  $Le_r^{\text{rms}} \sim (N/\Omega)^{-5/3} \sim 10^{-9}$ , where  $N$  here is the Brunt–Väisälä frequency including both thermal and compositional contributions (Fuller et al. 2019; Li et al. 2022, 2023). For AMRI, our numerical results indicate that  $Le_r^{\text{rms}}$  decreases less steeply with thermal stratification. However, the typical values we obtain at a moderate stratification of  $N = 20$  are  $Le_r^{\text{rms}} \sim 10^{-3}$ , which is already one order of magnitude lower than the smallest observed value.

Although AMRI turbulence seems unable to explain the strong magnetic fields observed in the core, we cannot exclude that weaker fields could be generated in the outer radiative regions of red giants, in particular above the hydrogen burning shell where  $N_T/\Omega$  is lower at  $\sim 10^2$  as discussed before. AMRI could also be triggered during earlier stages of the evolution of low-mass stars, for example during the core contraction phase immediately after the main sequence. Numerical simulations suggest that large scale fields, relic of a core convective dynamo during the main sequence, can destabilize the differential rotation produced by core contraction through axisymmetric MRI (Gouhier et al. 2022).

Recent stellar evolution models indicate that MHD turbulence is required to reconcile the internal rotation of the Sun with its surface Li abundance and to reproduce the observed Li depletion of pre-main sequence and solar-type stars (Eggenberger et al. 2022). These models employ prescriptions for the transport by TI dynamo action where the turbulent Schmidt number scales as  $Sc_T \sim (N/\Omega)^2 \gg 1$ . We show that AMRI turbulence transports AM more efficiently than chemical elements, as suggested by these stellar evolution models, but  $Sc_T$  is too low at values of about 2 and does not show significant variations for the moderate degrees of thermal stratification explored.

In conclusion, we confirm that AMRI turbulence can strongly enhance the transport of AM and chemical elements in radiative stellar interiors and its efficiency may be higher than the one of TI. The turbulent viscosity moderately decreases with stable stratification and the chemical turbulent diffusion coefficient follows a similar scaling but is weaker in amplitude. While our numerical simulations capture the mild molecular diffusivity ratios of degenerate stellar cores, extensive parameter investigations are needed to robustly extrapolate the results at the extreme degrees of stratification that characterize stellar interiors. Further numerical studies in a spherical geometry exploring MRI-induced transport for different shear profiles and amplitudes than those examined here and considering chemical buoyancy could give additional insights on the rotational and chemical evolution of low-mass stars.

*Acknowledgements.* The authors acknowledge support from the project BEAMING ANR-18-CE31-0001 of the French National Research Agency (ANR). L.J. acknowledges support from the Institut Universitaire de France. This work was performed using high performance computing resources from CALMIP (Grants 2021A-P1118, 2021B-P1118, 2022A-P1118, 2022B-P1118 and 2023A-P1118) and from GENCI-IDRIS (Grants 2022-A0110410970 and 2023-AD0100413776). The authors are indebted to Sébastien Deheuvels and François Rincon for helpful discussions and thank an anonymous referee whose insightful comments have improved the quality of the manuscript.

## References

- Aerts, C., Mathis, S., & Rogers, T. M. 2019, *ARA&A*, 57, 35
- Arlt, R., Hollerbach, R., & Rüdiger, G. 2003, *A&A*, 401, 1087
- Balbus, S. A., & Hawley, J. F. 1992, *ApJ*, 400, 610
- Beck, P. G., Bedding, T. R., Mosser, B., et al. 2011, *Science*, 332, 205
- Bonanno, A., & Urpin, V. 2012, *ApJ*, 747, 137
- Bonanno, A., & Urpin, V. 2013, *A&A*, 552, A91
- Brun, A. S., & Toomre, J. 2002, *ApJ*, 570, 865
- Cantiello, M., Mankovich, C., Bildsten, L., Christensen-Dalsgaard, J., & Paxton, B. 2014, *ApJ*, 788, 93
- Charbonnel, C., Lagarde, N., Jasniewicz, G., et al. 2020, *A&A*, 633, A34
- Christensen, U. R., & Aubert, J. 2006, *Geophys. J. Int.*, 166, 97
- Christensen, U., & Wicht, J. 2007, *Core Dynamics*, (Elsevier) 8, 245
- Deheuvels, S., Doğan, G., Goupil, M. J., et al. 2014, *A&A*, 564, A27
- Deheuvels, S., Li, G., Ballot, J., & Lignières, F. 2023, *A&A*, 670, L16
- Deliyannis, C. P. 2000, *ASP Conf. Ser.*, 198, 235
- Dormy, E., & Soward, A. M. 2007, *Mathematical Aspects of Natural Dynamos* (Chapman and Hall/CRC)
- Dumont, T., Charbonnel, C., Palacios, A., & Borisov, S. 2021, *A&A*, 654, A46
- Eggenberger, P., Montalbán, J., & Miglio, A. 2012, *A&A*, 544, L4
- Eggenberger, P., den Hartogh, J. W., Buldgen, G., et al. 2019, *A&A*, 631, L6
- Eggenberger, P., Buldgen, G., Salmon, S. J. A. J., et al. 2022, *Nat. Astron.*, 6, 788
- Fromang, S., Papaloizou, J., Lesur, G., & Heinemann, T. 2007, *A&A*, 476, 1123
- Fuller, J., Lecoanet, D., Cantiello, M., & Brown, B. 2014, *ApJ*, 796, 17
- Fuller, J., Piro, A. L., & Jermyn, A. S. 2019, *MNRAS*, 485, 3661
- Garaud, P., Medrano, M., Brown, J. M., Mankovich, C., & Moore, K. 2015, *ApJ*, 808, 89
- Gehan, C., Mosser, B., Michel, E., Samadi, R., & Kallinger, T. 2018, *A&A*, 616, A24
- Goossens, M., & Tayler, R. J. 1980, *MNRAS*, 193, 833
- Goossens, M., Biront, D., & Tayler, R. J. 1981, *Ap&SS*, 75, 521
- Gouhier, B., Lignières, F., & Jouve, L. 2021, *A&A*, 648, A109
- Gouhier, B., Jouve, L., & Lignières, F. 2022, *A&A*, 661, A119
- Gressel, O. 2010, *MNRAS*, 405, 41
- Griffiths, A., Eggenberger, P., Meynet, G., Moyano, F., & Aloy, M.-Á. 2022, *A&A*, 665, A147
- Guseva, A., Hollerbach, R., Willis, A. P., & Avila, M. 2017a, *Phys. Rev. Lett.*, 119, 164501
- Guseva, A., Willis, A. P., Hollerbach, R., & Avila, M. 2017b, *ApJ*, 849, 92
- Hawley, J. F., Guan, X., & Krolik, J. H. 2011, *ApJ*, 738, 84
- Hawley, J. F., Richers, S. A., Guan, X., & Krolik, J. H. 2013, *ApJ*, 772, 102
- Hollerbach, R., Teeluck, V., & Rüdiger, G. 2010, *Phys. Rev. Lett.*, 104, 044502
- Jouve, L., Gastine, T., & Lignières, F. 2015, *A&A*, 575, A106
- Jouve, L., Lignières, F., & Gaurat, M. 2020, *A&A*, 641, A13
- Käpylä, P. J., & Korpi, M. J. 2011, *MNRAS*, 413, 901
- Kirillov, O. N., Stefani, F., & Fukumoto, Y. 2012, *ApJ*, 756, 83
- Lesur, G., & Longaretti, P. Y. 2007, *MNRAS*, 378, 1471
- Li, G., Deheuvels, S., Ballot, J., & Lignières, F. 2022, *Nature*, 610, 43
- Li, G., Deheuvels, S., Li, T., Ballot, J., & Lignières, F. 2023, *A&A*, 680, A26
- Lignières, F., Califano, F., & Mangeney, A. 1999, *A&A*, 349, 1027
- Lodders, K., Palme, H., & Gail, H. P. 2009, *Landolt-Börnstein, New Series*, 4B, 560
- Mamatsashvili, G., Chagelishvili, G., Pessah, M. E., Stefani, F., & Bodo, G. 2020, *ApJ*, 904, 47
- Marques, J. P., Goupil, M. J., Lebreton, Y., et al. 2013, *A&A*, 549, A74
- Masada, Y., Sano, T., & Takabe, H. 2006, *ApJ*, 447, 447
- Meduri, D. G., Lignières, F., & Jouve, L. 2019, *Phys. Rev. E*, 100, 013110
- Miesch, M. S. 2005, *Liv. Rev. Sol. Phys.*, 2, 1
- Moyano, F. D., Eggenberger, P., Meynet, G., et al. 2022, *A&A*, 663, A180
- Moyano, F. D., Eggenberger, P., Mosser, B., & Spada, F. 2023, *A&A*, 673, A110
- Ogilvie, G. I., & Pringle, J. E. 1996, *MNRAS*, 279, 152
- Petitdemange, L., Marcotte, F., & Gissinger, C. 2023, *Science*, 379, 300
- Pinçon, C., Belkacem, K., Goupil, M. J., & Marques, J. P. 2017, *A&A*, 605, A31
- Pitts, E., & Tayler, R. J. 1985, *MNRAS*, 216, 139
- Reboul-Salze, A., Guilet, J., Raynaud, R., & Bugli, M. 2021, *A&A*, 645, A109
- Reboul-Salze, A., Guilet, J., Raynaud, R., & Bugli, M. 2022, *A&A*, 667, A94
- Rincon, F. 2019, *J. Plasma Phys.*, 85, 205850401
- Rincon, F., Ogilvie, G. I., & Proctor, M. R. E. 2007, *Phys. Rev. Lett.*, 98, 254502
- Rincon, F., Ogilvie, G. I., Proctor, M. R. E., & Cossu, C. 2008, *Astron. Nachr.*, 329, 750
- Riols, A., Rincon, F., Cossu, C., et al. 2013, *J. Fluid Mech.*, 731, 1
- Rüdiger, G., Hollerbach, R., Gellert, M., & Schultz, M. 2007, *Astron. Nachr.*, 328, 1158
- Rüdiger, G., Gellert, M., Schultz, M., Hollerbach, R., & Stefani, F. 2013, *MNRAS*, 438, 271
- Rüdiger, G., Gellert, M., Spada, F., & Tereshin, I. 2015, *A&A*, 573, A80
- Schaeffer, N. 2013, *Geochem. Geophys. Geosyst.*, 14, 751
- Schmid, P. J. 2007, *Annu. Rev. Fluid Mech.*, 39, 129
- Shi, J., Krolik, J. H., & Hirose, S. 2010, *ApJ*, 708, 1716
- Simon, J. B., & Hawley, J. F. 2009, *ApJ*, 707, 833
- Spada, F., Gellert, M., Arlt, R., & Deheuvels, S. 2016, *A&A*, 589, A23
- Spruit, H. C. 1999, *A&A*, 349, 189
- Spruit, H. C. 2002, *A&A*, 381, 923
- Squire, J., & Bhattacharjee, A. 2014, *ApJ*, 797, 67
- Talon, S., & Charbonnel, C. 2008, *A&A*, 482, 597
- Tayler, R. J. 1973, *MNRAS*, 161, 365
- Velikhov, E. P. 1959, *J. Exptl. Theoret. Phys.*, 36, 1398
- Wheeler, J. C., Kagan, D., & Chatzopoulos, E. 2015, *ApJ*, 799, 85
- Wicht, J. 2002, *Phys. Earth Planet. Int.*, 132, 281

## Appendix A: Taylor instability

As mentioned in Sect. 4.1, we observe TI in two of our unstratified simulation runs at  $\text{Pm} = 1$ . Here we provide evidence of this instability in run U4 at  $\text{Re} = 5 \times 10^3$  and  $\text{Ha}_\phi^{\text{max}} = 5012$ .

TI is a pinch-type instability of purely toroidal fields expected to occur in radiative stellar interiors (Taylor 1973; Spruit 1999). In spherical coordinates, Goossens & Taylor (1980) studied the adiabatic stability of weak axisymmetric toroidal fields  $B_\phi(r, \theta)$  when no rotation is present using an energy method. The toroidal field  $B_\phi$  has arbitrary radial dependence and angular dependence  $(1 - x^2)^{1/2} dP_\ell/dx$ , where  $x = \cos \theta$  and  $P_\ell$  is the Legendre polynomial of degree  $\ell$ . The field is weak in the sense that the magnetic pressure is much smaller than the hydrostatic pressure, so that it does not modify the basic stellar equilibrium. A necessary and sufficient condition for non-axisymmetric instability is (Goossens et al. 1981)

$$B_\phi^2 (m^2 - 2 \cos^2 \theta) - \sin \theta \cos \theta \frac{\partial B_\phi^2}{\partial \theta} < 0. \quad (\text{A.1})$$

The instability is most likely for azimuthal modes  $|m| = 1$  and for large latitudinal gradients of  $B_\phi^2$ . A Taylor expansion easily shows that the regions close to the poles ( $|x| \ll 1$ ) are always unstable for  $|m| = 1$ . Away from the poles, instability can also occur but only if  $B_\phi^2$  increases sufficiently rapidly with  $x$ . The growth rate of the most unstable mode  $m_{\text{max}}^{\text{TI}} = 1$  is on the order of the toroidal Alfvén frequency  $\omega_A = B_\phi / (\mu_0 \rho)^{1/2} r \sin \theta$  (Taylor 1973; Goossens et al. 1981). Rotation has a stabilizing influence on TI. Although not removing the instability, it reduces its maximum growth rate to (Pitts & Taylor 1985; Bonanno & Urpin 2013)

$$\gamma_{\text{max}}^{\text{TI}} = \omega_A^2 / \Omega. \quad (\text{A.2})$$

Figure A.1 displays the temporal evolution of the toroidal and poloidal magnetic energies of the spherical harmonic orders  $0 \leq m \leq 10$  for run U4. The nonaxisymmetric perturbations grow exponentially after about 2 system rotations from the perturbation time  $t_{\text{pert}} = 33.2$ . The most unstable azimuthal mode is  $m = 1$  (solid purple lines) as expected for TI. Its linear growth rate is  $\gamma_{\text{max}} / \Omega_a \approx 1.9$  and  $1.6$  when calculated over the time interval  $t - t_{\text{pert}} = 2 - 4$  of the rms toroidal and poloidal field evolutions respectively (cf. black dashed lines in Fig. A.1).

The instability saturates at  $t - t_{\text{pert}} \approx 12$  when the rms nonaxisymmetric toroidal field strength is roughly 5 times lower than the one of the axisymmetric toroidal field  $\bar{B}_\phi$  and about 2 times higher than the nonaxisymmetric poloidal one. We observe the generation of axisymmetric poloidal field  $\bar{B}_p$  due to the flow and field instability fluctuations at a rate which is roughly twice the one of the  $m = 1$  mode (solid black line in Fig. A.1b). After saturation, the instability decays on longer times not shown in Fig. A.1.

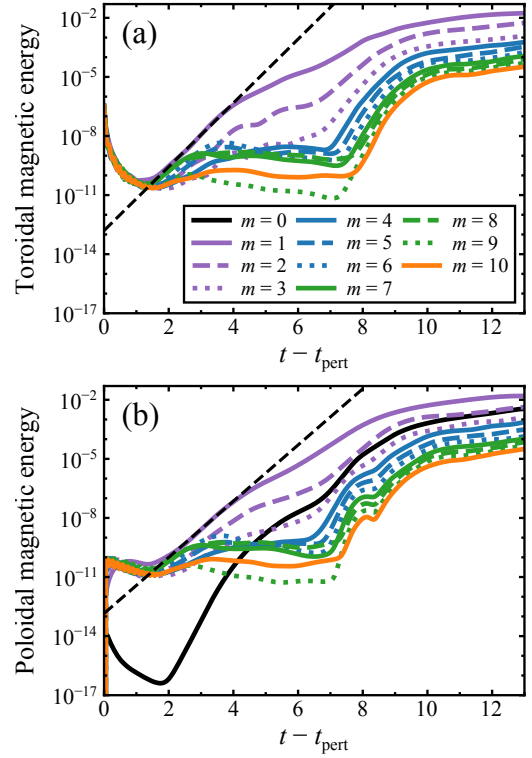


**Fig. A.1.** Temporal evolution of the (a) toroidal and (b) poloidal magnetic energies of the azimuthal modes  $m = 0 - 10$  for run U4 ( $\mathcal{N} = 0$ ,  $\text{Re} = 5 \times 10^3$ ,  $\text{Pm} = 1$ , and  $\text{Ha}_\phi^{\text{max}} = 5012$ ). The black dashed lines show linear fits of the energies of the most unstable mode  $m = 1$  over the interval  $2 \leq t - t_{\text{pert}} \leq 4$  covering the linear phase of the instability growth. These fits provide the growth rates  $\gamma_{\text{max}} / \Omega_a$  of the  $m = 1$  rms toroidal and poloidal fields, which are 1.9 and 1.6 respectively.

During its linear growth, the instability is localized close to the poles, but also around the central equatorial regions of the fluid domain (Fig. A.2a,b). For the axisymmetric azimuthal field configuration  $\bar{B}_\phi$  that we perturbed (Fig. A.2c), the instability condition (A.1) predicts, in addition to the classical wedge-shaped regions around the poles, several other unstable locations dispersed at lower latitudes, which originate from locally high latitudinal gradients of the field (gray shaded areas in Fig. A.2d). The unstable central equatorial regions correlate with the locations where the expected growth rates  $\gamma_{\text{max}}^{\text{TI}}$  from Eq. (A.2) are larger (Fig. A.2d) and where the instability is also observed. At these locations  $\gamma_{\text{max}}^{\text{TI}} / \Omega_a \approx 1.3$ , which agrees well with the growth rate  $\gamma_{\text{max}}$  of the  $m = 1$  mode observed in the simulation run.

We also observe TI in the unstratified run at  $\text{Re} = 10^4$  and  $\text{Ha}_\phi^{\text{max}} = 9787$  (Fig. 4) and we obtain similar results in the analysis of the linear instability growth that we therefore do not discuss here.

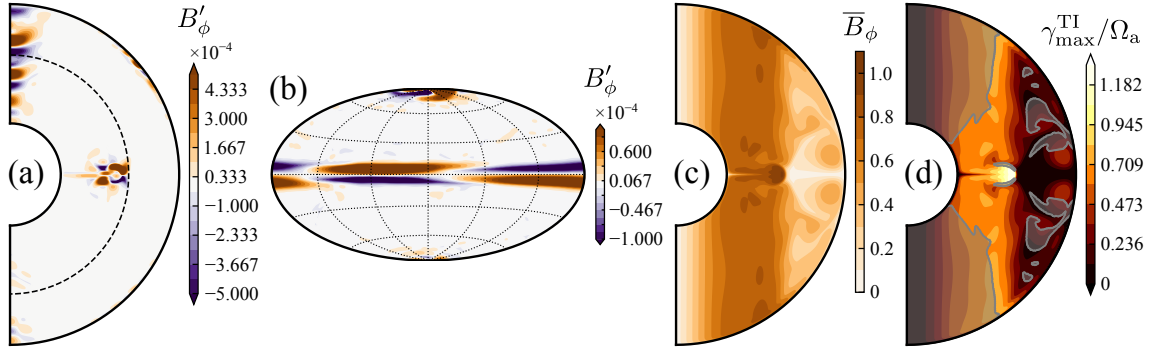


**Fig. A.2.** Taylor instability in run U4 and comparison with local linear analysis predictions. (a) Meridional cut and (b) surface projection of the nonaxisymmetric azimuthal field  $B'_\phi$  at time  $t - t_{\text{pert}} = 3.5$  during the linear phase of the instability growth. The surface projection is taken at radius  $r/r_o = 0.7$ , which is indicated by the dashed line in (a). (c) Axisymmetric azimuthal field  $\bar{B}_\phi$  at the perturbation time  $t_{\text{pert}} = 33.2$ . (d) Theoretical TI growth rate  $\gamma_{\text{max}}^{\text{TI}} = \omega_A^2/\Omega$ . The gray shaded areas show the locations where the instability condition (A.1) for the  $m = 1$  mode and the axisymmetric azimuthal field solution in (c) is fulfilled.

## Appendix B: Free azimuthal flow evolution of the fiducial dynamo run U0

Here we confirm that a net outward transport of AM is induced by AMRI, as already anticipated by the analysis of Sect. 6, performing a numerical experiment where the azimuthal flow is free to evolve.

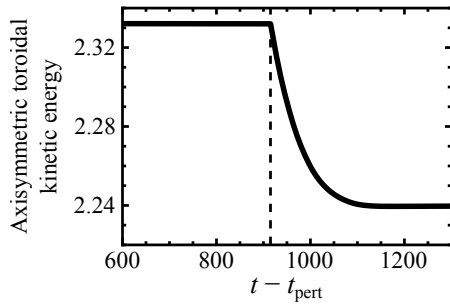


**Fig. B.1.** Axisymmetric toroidal kinetic energy as a function of time for the unstratified fiducial dynamo run U0 when the azimuthal flow is free to evolve. The azimuthal flow forcing is stopped ( $\mathbf{f} = \mathbf{0}$ ) at time  $t - t_{\text{pert}} = 915.0$  which is marked by the vertical dashed line.

Figure B.1 displays part of the temporal evolution of the axisymmetric toroidal kinetic energy in the quasi steady state of the unstratified fiducial dynamo run U0 ( $t - t_{\text{pert}} < 915$ ). At  $t - t_{\text{pert}} = 915.0$  (vertical dashed line), the azimuthal body force  $\mathbf{f}$  in the momentum equation (2) is set to zero. The azimuthal flow relaxes to a state of uniform rotation in a few hundreds of rotation times  $\tau_\Omega = 1/\Omega_a$ . Figure B.2 demonstrates that the initial cylindrical profile of the azimuthally averaged angular velocity  $\bar{\Omega}$  flattens over time under the influence of AMRI. The flow decelerates in the interior and accelerates in the outer regions, producing a net outward transport of AM, and reaches a state of almost rigid rotation at  $t - t_{\text{pert}} \approx 1200$ .

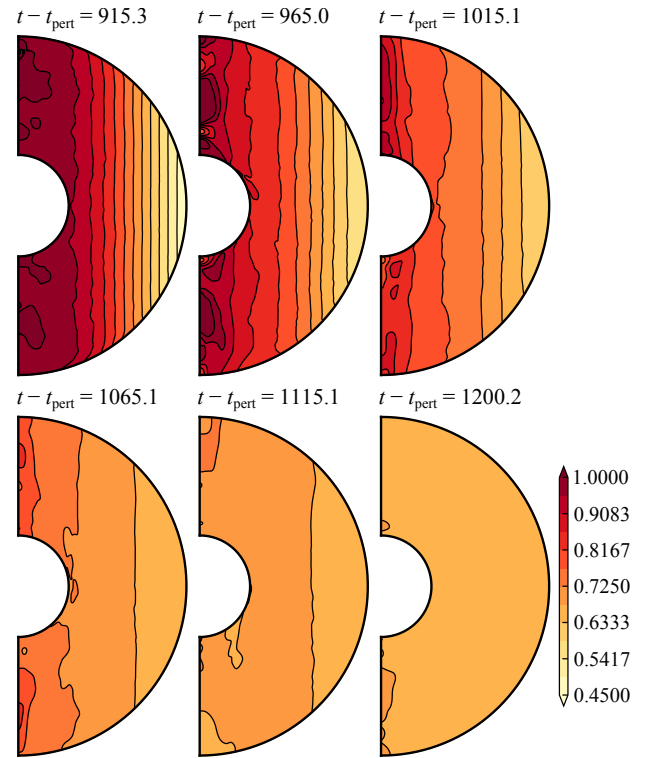


**Fig. B.2.** Snapshots of the azimuthally averaged angular velocity  $\bar{\Omega}$  during the free azimuthal flow evolution of run U0 ( $t - t_{\text{pert}} > 915$ ) shown in Fig. B.1.